TECHNICAL UNIVERSITY OF CRETE
SCHOOL OF PRODUCTION ENGINEERING & MANAGEMENT
Turbomachines & Fluid Dynamics Laboratory (TurboLab-TUC)

The design of an aspirator device for the collection of olive fruits

Konstantinos Fytilis

Diploma Thesis

Supervisor: Prof. Dr. Ioannis K. Nikolos

Chania, April 2025

Contents

List of figures

List of tables

Chapter 1. Introduction

1.1. Process of olive fruits collection

The process of collecting olive fruits is considered as a heavy-duty and time-consuming job (*Figure* 1). In a quick overview, the process consists of two main tasks. Initially, a net is placed around the tree and the branches of the tree are shacked or smacked for the olive fruits to fall from the branches to the ground, where the net is placed. The second task is the collection of the fruits lying on the net in bags, or crates, for the olive fruits to be transported from the field. Both tasks need machinery assistance, to be less demanding and more time efficient.

After a quick search in the literature one can find agricultural machinery for assistance in both tasks. The first task of harvesting can be aided using electric-powered brushes that smack the fruits off the tree. A more highly automated solution involves the use of vibrational machinery, which vigorously shakes the entire tree, causing the fruits to dislodge from the branches. As for the second task, the collection of the fruits to the transporting units (sacks, crates) there also exists some machinery-aided solutions for reducing the labour part. Most of them are ad-hoc solutions due to the specific features of the tasks, depending on the field's morphology. A more robust solution for making that process less arduous and more efficient is by using an aspirator device.

Figure 1: Aspirator device on the field, during the collection of olive fruits. [Source: Youtube video - Agrioil aspiratore idraulico raccolta olive]

The aspirator uses air suction to pick up the fruits from the net and dispose them in the collecting units, rather than collect the fruits of the net by hand. The use of the aspirator in this task, not only makes it less demanding for the workers, but it also saves labour time, as this machine can be operated even by one person, rather than multiple workers when it is done manually, thus reducing labour cost.

1.2. Aspirator device

The aspirator device (*Figure* 2) is composed of the collecting box, where the olive fruits are gathered, the hose that is actually a flexible pipe (hose), enabling the worker to collect the olive fruits, and the impeller's assembly, responsible for generating the suction airflow. The last part is the driving force of the aspirator. In more detail, an air blower is rotated by the power unit (usually the tractor’s engine), and an air flow is induced, due to the under-pressure (suction). Therefore, the hose can collect the olive fruits from the net, using the air flow and dispose them into the collecting bin.

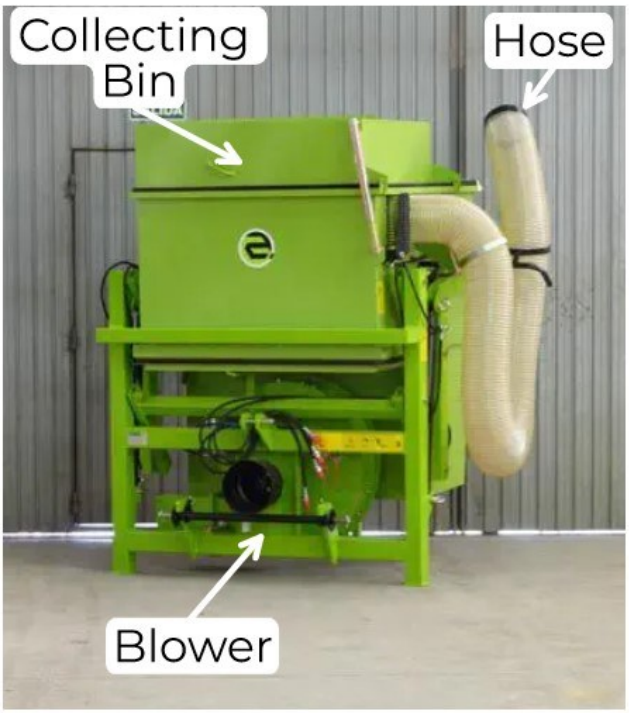

Figure 2: Aspirator components [Source: www.agriexpo.online]

The aspirator assembly can offer extra features, such as deleafing device, meaning the extraction of olive tree's leaves from the pile collected on the net, so only the olive fruits are collected. To implement the above feature, the collecting bin of the aspirator must be modified, so when the pile is forced through the hose and transferred to the bin, there will be a separation of the solid material's flow between the leaves and olive fruits. In this case the collecting bin is a cyclone, to wit a cylindrical barrel, which utilizes the lighter weight of the leaves compared to the heavier olive fruits, driving the flow of the solid particles of the olive fruits downwards to the bin and the leaves (following the air flow) towards the exit of the casing of the impeller (*Figure* 3).

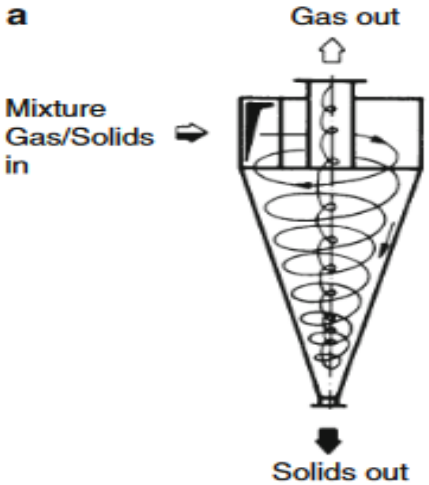

Figure 3: Cyclone's operation. It can be utilized to separate the olive leaves from the solids (olive fruits). [Source: Pneumatic conveying of solids. Ch.10]

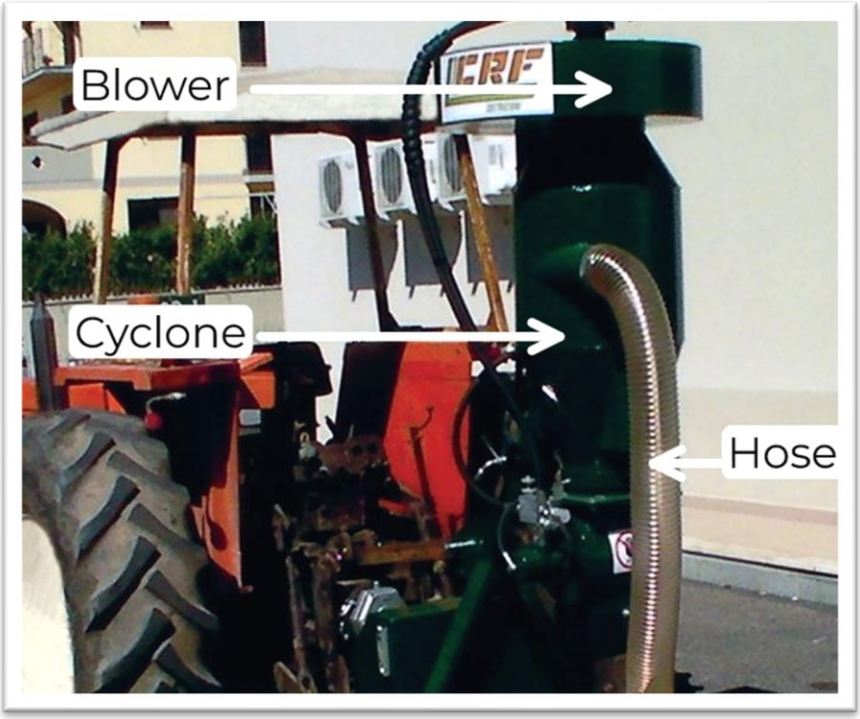

Figure 4: Aspirator device with Cyclone. [Source: crfcostruzioni.it]

Some other features that the aspirator assembly could offer regard the olive fruits storage. The collecting bin could have the ability to be risen using hydraulic cylinders, so the payload can be unloaded. An alternative solution could be a hydraulic or mechanical gate at the bottom of the bin that helps the olive fruits to unload.

While the concept of the aspirator machine is straightforward, the design and implementation pose challenges, due to the intricate airflow generated by the centrifugal impeller. The complexity of the airflow stems from the elaborate geometry of the air domain, particularly in the case of the cyclone aspirator, and the fact that the flow is not a single-phase flow but rather a complex two-phase mixture of air and large solid particles. In addition, the bulk density of the solid phase (not the density of a single particle) cannot be predetermined, due to the multiple forces acting on the solid particles and the air-solid interactions, as seen in *Figure* 5.

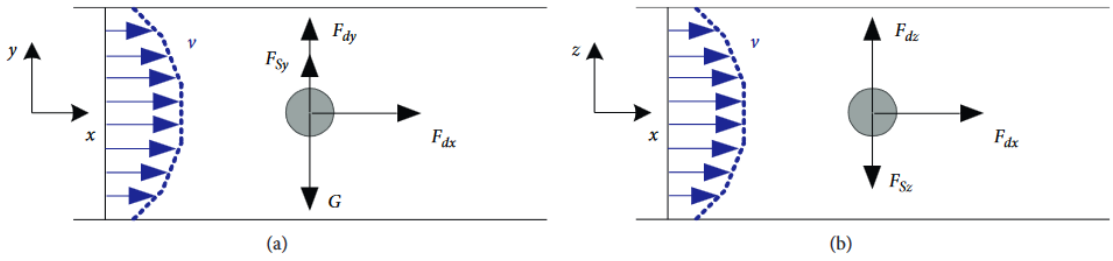

Figure 5: Forces acting on a solid particle that is transported due to an airstream. [Source: Research article, "Prediction of Horizontal Pneumatic Conveying of Large Coal Particles Using Discrete Phase Model"] (1)

The forces acting on a solid particle carried due to airstream, as shown in the figure above, are the drag force F_d, the gravitational force G and the boyuoancy force F_s. In addition, a particle interacts with other solid particles and the pipe walls due to collisions, as shown in the following *Figure* 6.

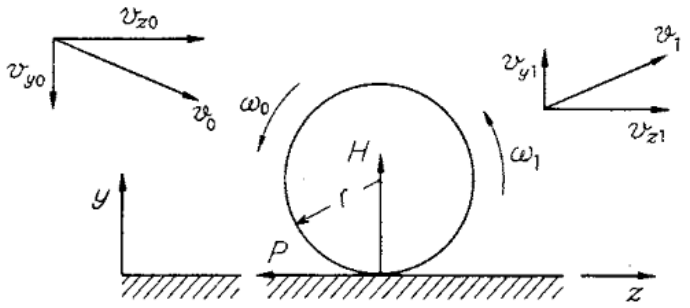

Figure 6: Change of the velocity components of a spherical solid particle due to wall collision. [Source: "PNEUMATIC CONVEYING OF SOLIDS THROUGH STRAIGHT PIPES"] [6]

The attempt to construct an analytical solution for the two-phase flow, for determining the necessary air flow that the impeller must induce for the transportation of the olive fruits, or the olive fruit flow that will be generated, is a very complex task. Research on related topics involves the investigation of the necessary velocity for pneumatic conveying of finer particles at the range of the micrometers (μm). In those diameter regimes, the inertia forces are not as influential as they are for the olive fruits. The dominant forces are the viscosity and coherence forces. Furthermore, the olive fruits shape is not isotropic, so its orientation relevant to the air flow direction changes the direction of the lift forces, which are more dominant compared to the micrometer regime. Also, the orientation of the olive fruit due to random collisions with other olive fruits and the wall changes in an unpredicted fashion. In conclusion, the most efficient way for making progress with the calculation is with simulations, experiments and manipulation experimental data obtained from previous trials.

1.3. Purpose of this project

The aspirator machine falls within the domain of commercial agricultural machinery, and being a relatively new device, there is a lack of documentation and extensive bibliography, regarding its design parameters. In addition, there is no experimental data of olive fruits pneumatic conveying, as the only extended bibliographic research of dilute phase pneumatic conveying of large particles (cm regime) is for large coal particles [1]. Therefore, the purpose of this project is to register a bibliographic reference for the aspirator device operation and working principles. Moreover, to write down the theoretical background for the designing process of the aspirator device.

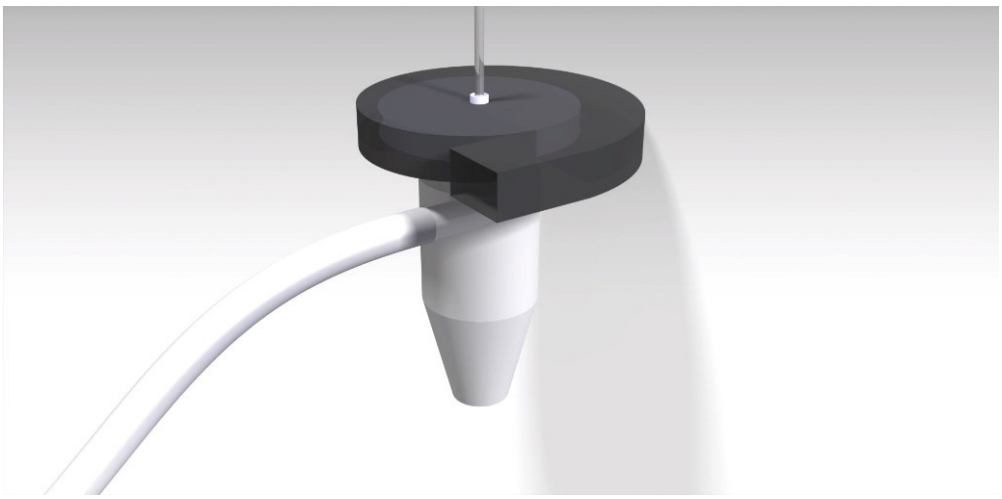

Figure 7: Aspirator device's assembly designed in CAD software.

As previously mentioned, the approach of obtaining insights for designing the aspirator device involves the manipulation of empirical data from prior endeavours. Experimental data can resolve empirical equations from interpolation of the experimental data and from similarity laws. The author initiated an effort to design an aspirator device with no previous experimental data in his possession. The components were initially chosen for the construction of an aspirator device with a cyclone, as presented in Figure 7: Aspirator device's assembly designed in CAD software.*Figure* 7.

The choice to include a cyclone was motivated by its ability to achieve two critical goals: firstly, to separate the olive fruits solid particles from the air stream, before the flow reaches the impeller's inlet, and secondly, to facilitate the separation of olive leaves from the collected olive fruits. The parameter's selection was mainly based on reverse engineering methods, due to the lack of experimental data; therefore only a few of the mathematical formulas found in bibliography could be applied. Further analysis of the reasons for choosing the initial setup of the aspirator device and its parameter's selection can be found in sections *3.3* and *3.53.5*. It's important to note that the outcomes of the initial endeavor were reasonably good, in terms of solid particle transport, although there was room for improvement. Additionally, the performance in separating leaves from the collected olive fruits was not as satisfactory. Some data were also gathered during this process, which is elaborated upon in section *3.63.6*.

It will become evident in the following sections that these data alone are insufficient for a comprehensive analysis of the operating conditions of the aspirator device. One crucial variable is the solid particles velocity *c* and the pressure drop for the solid particles motion, but unfortunately this variable can be experimentally calculated only with sophisticated experimental setup, such as high-speed cameras or Laser-Doppler Velocimetry.

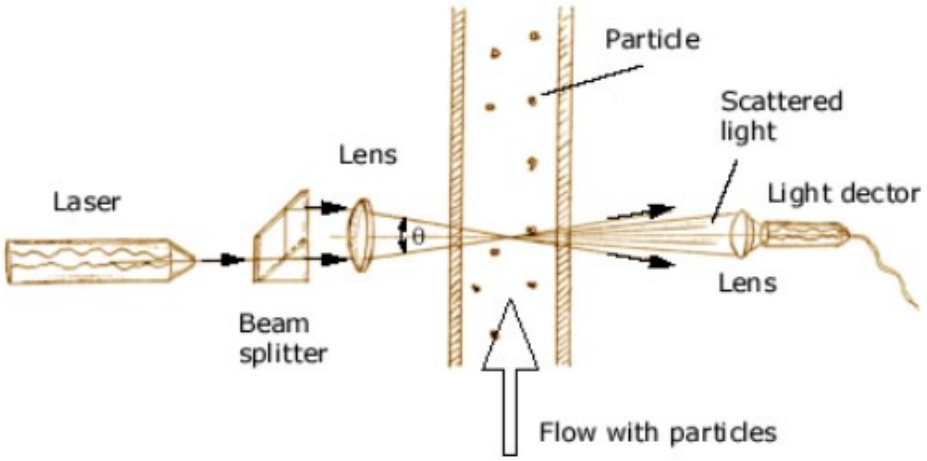

Figure 8: Laser doppler velocimetry setup. [Source: https://velocimetry.net/ldv_principles.htm]

To enhance the performance of the aspirator device, the author embarked on a second project aimed at constructing an aspirator device with a different setup. In this second design iteration, the cyclone was substituted with a straightforward, sizable rectangular box, which was employed as both a collecting bin and a separator for solid particles. Therefore, the function of expelling olive leaves was abandoned, as observations made during the operation of the first aspirator device with a cyclone indicated a diminished suction efficiency and an inefficient expulsion of the leaves. The following figure (Figure 9: Aspirator device's assembly with rectangular bin designed in CAD software.*Figure* 9*),* demonstrates the components of the aspirator device and the geometry of the rectangular collecting box.

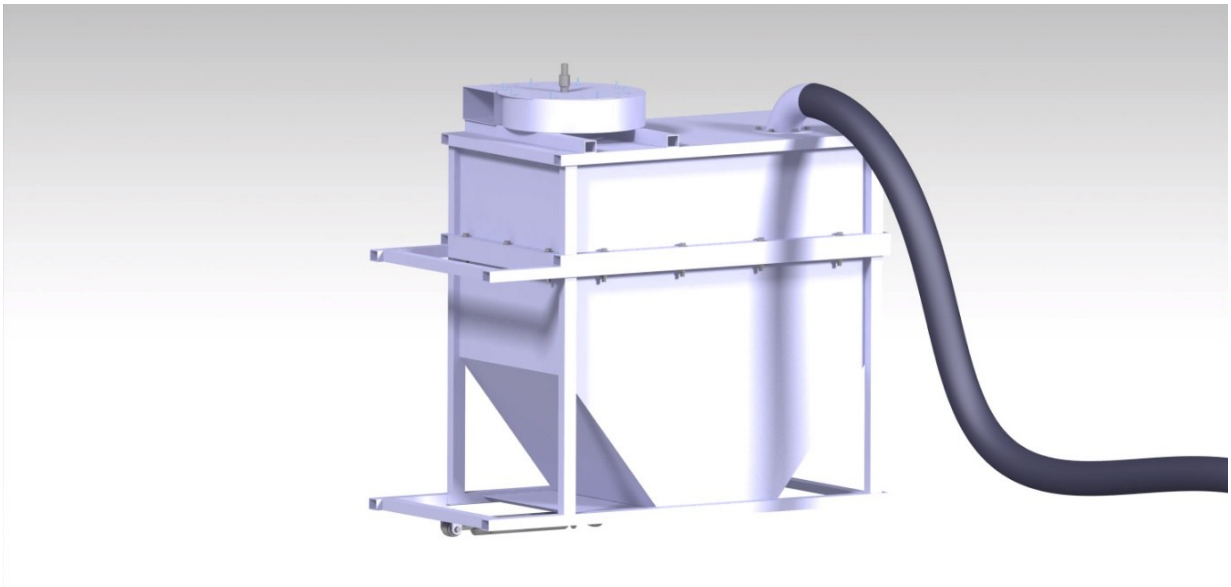

Figure 9: Aspirator device's assembly with rectangular bin designed in CAD software.

During the operation of the aspirator device with a rectangular box, operational data was collected, and insightful observations were made. These observations served as the foundation for some necessary modifications. The systematic presentation of the design process for the second design trial is detailed in section *3.8*. Prior to plunging into the design process and the results of the aspirator device, the following chapter will present the theoretical framework related to the aspirator device.

Chapter 2. Theory

2.1. Power equation

The starting point for designing the aspirator device is the determination of the power that is needed to feed the air mover component, so the induced air stream can transfer enough momentum to achieve the desired solid mass rate flow. The power equation for the air stream is the following:

$$Power = \Delta p * Q = \rho g \, H \, Q \tag{2.1}$$

When the air stream has achieved a steady state, the head H that is present in the piping system will be the same as the one induced by the air mover.

The Δp term corresponds to the pressure drop that the impeller must overcome for the desired air flow Q and the olive fruit mass flow $\dot{m}_{solid}$, to be induced. The Δp term, includes numerous phenomena that correspond to pressure drop, which are listed in section *2.4*. Taking into consideration the solid mass flow, the particle's size, and the air flow, it will be decoded which of these phenomena can be neglected. The formulas in section *2.4* will indicate that evaluating the power of the aspirator device based on the piping system is challenging due to the lack of experimental data needed to calculate the corresponding pressure drop.

Instead, the evaluation begins with the air mover. An important note is that the above equation gives the power that the fluid receives from the air mover (meaning the energy gain between suction and discharge of the air mover), not the power that is produced from the power unit driving the air mover. This power can be determined only if the coefficients of mechanical, hydraulic and volumetric efficiency are computed.

The air mover for the aspirator device will be a centrifugal impeller, since the compression and flow needed for the aspirator device function falls in the realm of blowers. A back-curved (two-dimensional) blade design is chosen for the impeller, due to its higher efficiency across a wider range of operating conditions, its smoother performance curve, and its ease of manufacturing.

The head H and the flow Q can be linked to the speed triangles at the leading and trailing edge of the impeller's blade, along with the impeller design parameters, so this starting point will also help in the impeller design. The formulas that link the air velocities are to follow.

Assuming that the entering air to the impeller has no tangential speed component ($c_{u1} \approx 0$), the Euler equation for turbomachines is the following:

$$H_u = \frac{1}{g} u_2 c_{u2} \tag{2.2}$$

where H_u is the theoretical head pressure, meaning the energy of a unit air volume in terms of meters of fluid height, that the fluid receives from the impeller without considering the head loss ΔH_t inside the impeller. Using the relation between head pressure and power:

$$Power_u = \rho_{air} \, g \, Q_u \, H_u \tag{2.3}$$

The same applies for the flow rate Q_u, as phenomena of recirculation inside the impeller occur due to various pressure gradients. Results in the following equation:

$$Power_u = \rho_{air} \;\; Q_u \, u_2 c_{u2} \tag{2.4}$$

As mentioned before, this represents the theoretical energy received by the fluid, not the actual power transmitted by the impeller. However, it serves as a useful starting point. To use the above formulas effectively, another assumption will be made, that the impeller operates at its optimum working point, where the air velocity triangle follows the blade angles, and no slip is occurring between the air and the impeller blade at the trailing edge. Therefore, the tangential speed at the trailing edge will be noted as the ideal tangential speed $c_{u2\infty}$.

The following relation links the tangential air velocity with the radial velocity and the trailing-edge linear speed:

$$c_{u2\infty} = u_2 - \frac{c_{r2}}{\tan\beta_2} \tag{2.5}$$

The radial air velocity is related to the impeller design parameters and the air flow:

$$c_{r2} = \frac{Q_u}{(\pi D_2 - Z_B s_2) b_2} \tag{2.6}$$

Finally, the air flow relates to impeller design parameters and the leading-edge linear velocity.

$$Q_u = u_1 \tan(\beta_1) * (\pi D_1 - Z_B s_1) b_1 \tag{2.7}$$

Using the formulas $(2.5) - (2.7)$, $c_{u2\infty}$ can be obtained only by the impeller design parameters, like the inlet and outlet diameter D_1, D_2, the blade width at inlet and outlet b_1, b_2, the blade angle at the leading and trailing edges β_1, β_2 and the rotational speed (in rpm) of the impeller.

Hence, the ideal Head $H_{u,i} = \frac{1}{g} u_2 c_{u2,\infty}$ can be calculated. In addition, the slip velocity can be modeled by the following formula:

$$w_{s2} = x * u_2 \tag{2.8}$$

where the coefficient x, can be retrieved by the $Pfleiderer$ formula:

$$x = 2k \frac{g H_{u,i}}{u_2} \frac{1}{Z_B \left[1 - \left(\frac{D_1}{D_2}\right)^2\right]} \quad where \;\; k = 0.6[1 + \sin(\beta_2)] \tag{2.9}$$

The calculation of the slip velocity can be achieved only by the impeller design parameters and the impeller's rotational speed (rpm), so the theoretical head H_u can be computed:

$$H_u = \frac{1}{g} u_2 \left(c_{u2,\infty} - w_{s2}\right) \tag{2.10}$$

2.2. Pneumatic conveying

The aspirator device has similarities with a pneumatic conveying system (*Figure* 10), as both use air flow to transport the solid particles. The two devices share the same components, such as the exhaust impeller (vacuum conveying), the piping system and the collecting bin (receiver). The only component that is not present in the aspirator device is the feeder. The feeder is a component that introduces solid material into the conveying system at a constant mass rate and simultaneously keeps the piping system sealed from the feeding bin. Hence, for the theoretical examination of the aspirator device, the theory of pneumatic conveying offers a relevant and applicable framework.

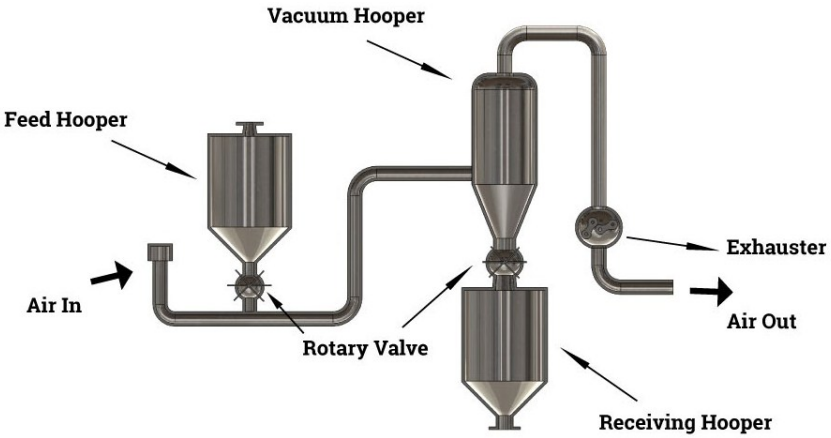

Figure 10: Vacuum pneumatic conveying system. [Source: www.iqsdirectory.com]

2.3. Dilute and dense phase conveying

The formulas of the pneumatic conveying theoretical framework rely on experimental data, so they may not apply in every flow condition, particle size, system geometry conveying phase. Furthermore, for a given set of parameters, multiple formulas are available, and their suitability for specific flow conditions may not always be evident, leaving uncertainties regarding the extent of deviation from real-world results.

The air flow modeling depends on whether the air flow is characterized as laminar or turbulent. In the same manner, the solid particle flow modeling relies on the characterization of the solid flow as dilute or dense. Each of the above categories will dictate which of the formulas can be applied.

The saltation velocity is a helpful quantity for making a distinction between dilute and dense phase. When the air stream velocity is above the critical value of the saltation velocity, the solid particles become suspended in the airflow, and they are uniformly dispersed in the cross-sectional area of the pipe, as shown in the following *Figure* 11.

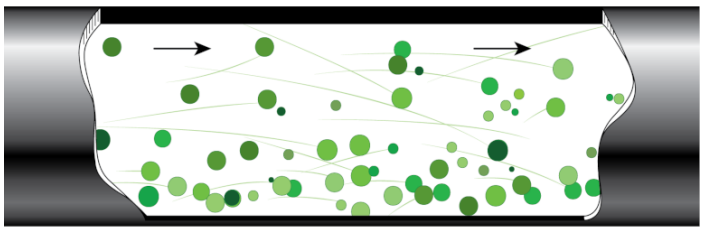

Figure 11: Particle motion in a dilute phase conveying regime. [Source: www.powderbulksolids.com]

As the air stream velocity reaches the saltation velocity, the solid particles start to fall out of the air stream and initially they form an aerated bed of particles, which is moving slowly if the material is fluidizable. This state of conveying is presented in the following *Figure* 12.

Figure 12: Mixed phase of conveying where the bottom section of the cross-sectional area of the pipe a bed of slowly moving particles is formed. [Source: www.powderbulksolids.com]

Further decrease of the air stream velocity below the saltation velocity results in a dense phase of conveying where the solid particles form plugs that move at a slow speed. This is necessary when the solid particles are abrasive or friable. Therefore, if the particles were moving at high velocities, the abrasive particles would damage the equipment and the friable solid particles would degrade. The plug-like form of the particles at dense conveying varies in correlation to the air permutability of the solid particles. When the solid particles are non-permutable to the air then the particles move in plugs that resemble a piston. The two different states of dense-phase conveying are presented in the following *Figure* 13.

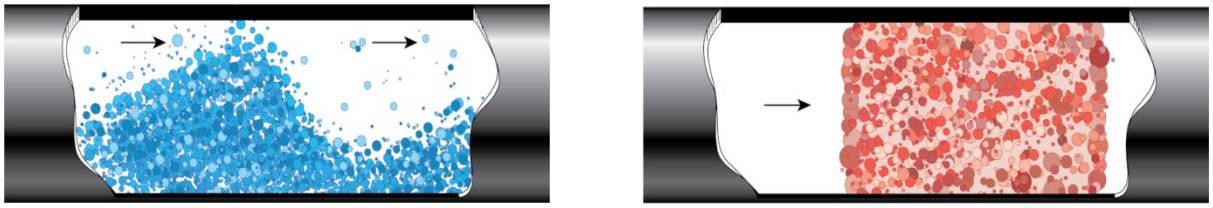

Figure 13: Dense phase conveying where the particles are air-permutable (left image) and non-permutable to air forming piston-like movement (right image). [Source: www.powderbulksolids.com]

The current effort undertaken by the author for the design of the aspirator device is focused on dilute-phase conveying for solid particles. This choice is based on the consideration that dilute conveying is more energy-efficient than dense-phase conveying and offers advantages in terms of modelling and predictability due to its extensive research background. Dense-phase conveying is typically reserved for situations involving abrasive or friable materials. Therefore, for the purposes of this study, a dilute-phase conveying assumption will be maintained.

2.4. Pressure loss modelling.

After clarifying the different states of the particle's motions inside the piping system and assuming dilute-phase conveying, the theoretical framework for pressure loss calculation is to follow. The assumption of dilute-phase conveying for the aspirator device is based on empirical observations from the author's previous trials. Even though the saltation velocity has not been calculated, which is the theoretical threshold between the two regimes, a common practice to distinguish the two regimes is by trials and empirical observations. Of course, there are a handful of theoretical approaches for the calculation of the saltation velocity [3]. Although, when the alternative of trial is available, it is the best

choice. Therefore, the author will conduct tests with some prototype setup to make some observations and then test the output of the saltation velocity formulas. The calculations are displayed in detail in section *3.2*.

The pressure losses are the result of the air to wall interactions, the particle-to-particle interactions and the particle to wall interactions. In dilute phase conveying it is possible to model those effects separately.

- Δp due to air friction:

The pressure drop due to air flow consists of major losses due to air-wall friction and minor losses due to bends in the piping system.

The major losses are modelled from the well-known formula:

$$\Delta p_l = f_D \frac{L}{D} \frac{\rho_{air} v^2}{2} \tag{2.5}$$

where the friction factor f_D is determined through empirical formulas or from Moody chart, when the air flow lies in the turbulence regime. The minor losses are due to piping elbows and fittings and are modeled as:

$$\Delta p_{l,minor} = \xi \frac{\rho_{air} v^2}{2} \tag{2.6}$$

- Δp due to particle friction and collision:

In dilute phase, the mechanism which enables the transfer of kinetic energy from the air to the solid particle is the aerodynamic drag. The energy losses arise from the particle-to-particle and particle-wall collisions and friction. It is difficult for those phenomena to be modelled separately, so both of those energy loss sources, in most cases, are modelled together in the bibliography. The formula for the pressure-drop due to solid particles collisions resembles the formula for the pressure drop due to airstream flow, as it is proportional to the square of the particle's velocity c, and proportional to a solid friction factor. The solid friction factor λ_z^*, is calculated using experimental data. A representation of the solid friction pressure drop is given below using the airstream velocity v and the mass flow ratio μ [3].

$$\Delta p_z = \mu \lambda_z \frac{\rho v^2}{2} \frac{\Delta L}{D} \tag{2.7}$$

where, λ_z is representing a function of the solid particles' velocity and friction:

$$\lambda_z = \frac{c}{v} \lambda_z^* + 2 \frac{v}{c} \frac{\beta}{Fr^2} \tag{2.8}$$

In the above equation, β is defined as $\beta = w_f / v$ and Fr represents the $Froude\ number$ which is a dimensionless number that is used to compare the inertia of the flow to the gravitational forces. In addition, bends in the piping system also increase the amount of pressure drop induced by the solid flow and are modelled separately.

- Δp due to vertical conveying:

The vertical transportation of solid particles to a greater height requires some work. That work is modeled via the pressure drop induced on the airstream. The formula for calculating the pressure loss due to vertical transportation is comparable to the head pressure drop, multiplied by some

coefficients that model the presence of the solid material, like the solid mass flow ratio and the ratio of solid to air velocity [3]:

$$\Delta p_{height} = \mu\ \rho\ g\ H \frac{v}{c} \tag{2.9}$$

- Δp due to bends, for two-phase flow:

Besides the minor losses, when the air stream navigates through a bend in the piping system, in two-phase flow the bends contribute further to pressure losses, as their geometry is acting like a phase separator. Moreover, it can diminish the solid particles' momentum. The pressure loss from bending is modelled as [3]:

$$\Delta p_{bend} = \frac{0.029 + 0.304\left[Re\left(\frac{D}{2R_b}\right)^2\right]^{-0.25}}{\left(\frac{2R_b}{D}\right)^{\frac{1}{2}}} \frac{L_b \rho v^2}{2D} \tag{2.10}$$

where, R_b is the curvature of the bend and L_b is the length of the bend. The Dean number $Re\left(\frac{D}{2R_b}\right)^2$ is present in the above formula. The biggest issue with using the above formula in the aspirator device design is that most of the bends in the piping system arise from the elastic hose formation, which changes constantly through operation and is eventually a stochastic event.

A useful insight is the fact that if the curvature of the hose results to a Dean number less than,

$$Re\left(\frac{D}{2R_b}\right)^2 < 0.034 \tag{2.11}$$

then, the bend is truly sweeping, and the straight pipe section pressure loss can be used instead.

- Δp due to particle acceleration:

All the previous investigations into the pressure losses assume that a steady state has been achieved. This is a reasonable assumption, as after an insignificant amount of time the system characteristic and the blower characteristic will intersect at the point of operation. Nevertheless, the acceleration of the solid particles must be modelled not over time but regarding the pipe's length, meaning as a function of distance. In simpler terms, air and solid flows have acceleration and deceleration regions in the piping system's entrances and exits, respectively. Given the fact that the aspirator device has a short length piping system, in comparison to most of the conveying systems, the development length could give a non-negligible contribution to the energy losses. Theoretically, addressing energy losses caused by acceleration entails solving a complex differential equation for the changing particle velocity and voidage. Given the complexity of this task, an experimental formula for energy losses due to acceleration, in which all the variables correspond to a steady-state situation, can be employed [3]:

$$\Delta p_{accelaration} = \mu \rho c v \tag{2.12}$$

2.5. Olive fruit data

To proceed with the calculations for the design of the aspirator device, it is imperative to acquire essential information about the conveyed solid particles, including their mass and shape. Olive fruits are available in numerous varieties, each exhibiting distinct densities and dimensions. To streamline the data collection process and optimize the design of the aspirator device for the specific geographical region in which it will operate, the olive fruit variety "Koroneiki" will be selected as the basis for data collection.

After a bibliographic search for the olive fruit properties [5], the following data were obtained:

Table 1: Olive fruit data

Fruit length (mm)	Fruit diameter (mm)	Fruit weight (gr)
19.8	11.91	1.53

To calculate the particle's density, the volume of the olive fruit will be calculated using the dimension data from the above table. The shape of the olive fruit will be modelled as a prolate spheroid, as shown in the following *Figure 14*.

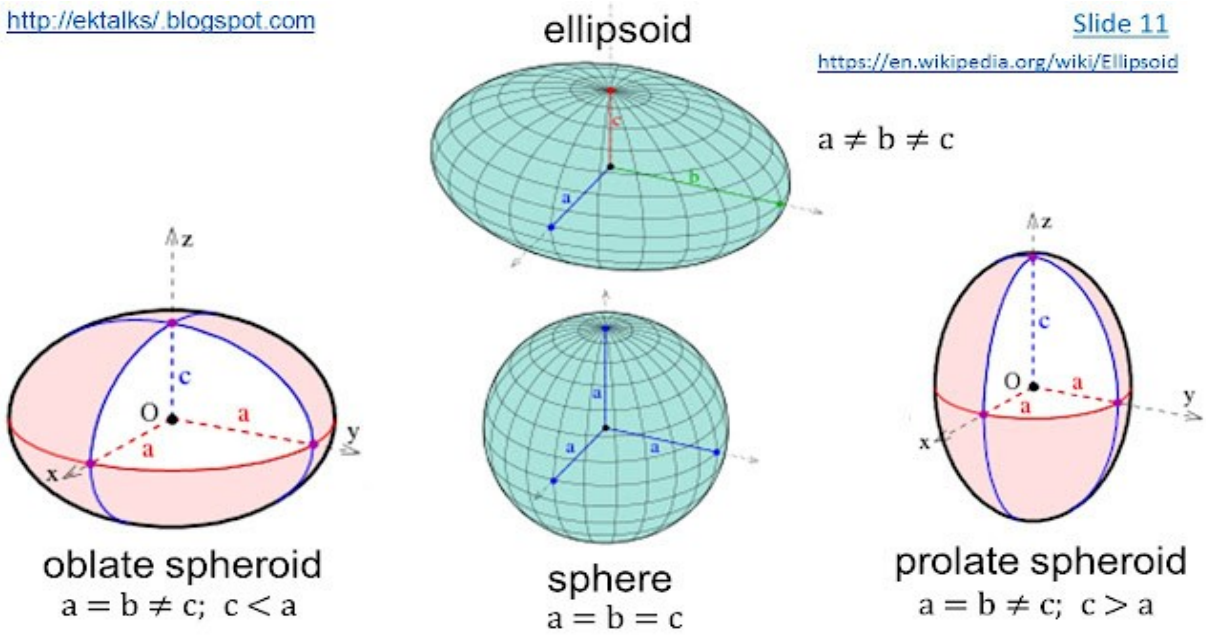

Figure 14: Spheroids - two of the axis have equal length. [Source: ektalks.blogspot.com]

The formula for the volume bounded by an ellipsoid:

$$V = \frac{4\pi abc}{3} \tag{2.13}$$

The volume of a single olive fruit is:

$$V_p = \frac{4\pi}{3} * (19.8mm) * (11.91mm)^2$$

$$V_p = 1468.12\ mm^3$$

From the volume of the olive fruit, the equivalent diameter can be calculated, as the diameter of a sphere with the same volume as the olive fruit. Therefore:

$$d = \left(\frac{3}{4\pi} V_p\right)^{\frac{1}{3}} \tag{2.14}$$

So,

$$d_p = 2\left(\frac{3}{4\pi} * 1462{,}12mm^3\right)^{\frac{1}{3}} = 14.1\ mm$$

The density of a single particle is:

$$\rho_p = \frac{m_p}{V_p} = \frac{1.53\ gr}{1468.12\ mm^3} = 1042.16\ kgr/m^3$$

Another useful quantity regarding the olive fruit geometry is the sphericity ψ, which is a ratio that exhibits how much a shape deviates from the spherical shape. It has a maximum value of 1, meaning a spherical shape. The definition of sphericity is:

$$\psi = \frac{surface\ area\ of\ spere\ with\ same\ volume\ as\ particle}{surface\ area\ of\ particle} \tag{2.15}$$

The formula for the surface area of a prolate spheroid ($a = b$), is:

$$S = 2\pi a^2\left(1 + \frac{c}{ae}\sin^{-1}(e)\right) \tag{2.16}$$

where $e^2 = 1 - \left(\frac{a}{c}\right)^2$

Substituting the data in the above equation, the surface area of the olive fruit is:

$$S_p = 651.26\ mm^2$$

The surface area of the sphere with diameter equal to the equivalent diameter of the olive fruit is:

$$S_{eq} = 624.68\ mm^2$$

So, the sphericity of the olive fruit is:

$$\psi = \frac{624.68}{651.26} = 0.959$$

Chapter 3. Design of the aspirator device

3.1. Aspirator device components selection

In the author's initial endeavor to design the aspirator device, the selection for the configuration and components included a back-curved blade centrifugal fan, a cyclone, and a plastic flexible hose. The back curved centrifugal fan was chosen because the back curved blades offer a more reliable and efficient operation over a wider range of air flows, as the operating point was not predetermined. The cyclone was chosen because it offers a robust solution for collecting the olive fruits at the bottom of the hopper. The cyclone can take advantage of the olive fruit's larger inertia relative to the air and separate the olive fruits from the air stream, before the air stream flows into the impeller's inlet. The most important reason for the usage of the cyclone was the feature of deleafing, meaning that the cyclone can also take advantage of the olive leaves' small inertia and their ability to interact strongly with the air stream. The olive leaves do not separate from the air flow and follow the stream into the impeller's inlet for the leaves to be expelled from the collecting hopper.

For each component, several design parameters had to be determined. For the back curved blade impeller, the following parameters had to be selected:

- Inlet diameter D_1, inlet blade width b_1
- Outlet diameter D_2, outlet blade width b_2
- Blade's leading-edge angel β_1
- Blade's trailing-edge angle β_2
- Rotational speed n

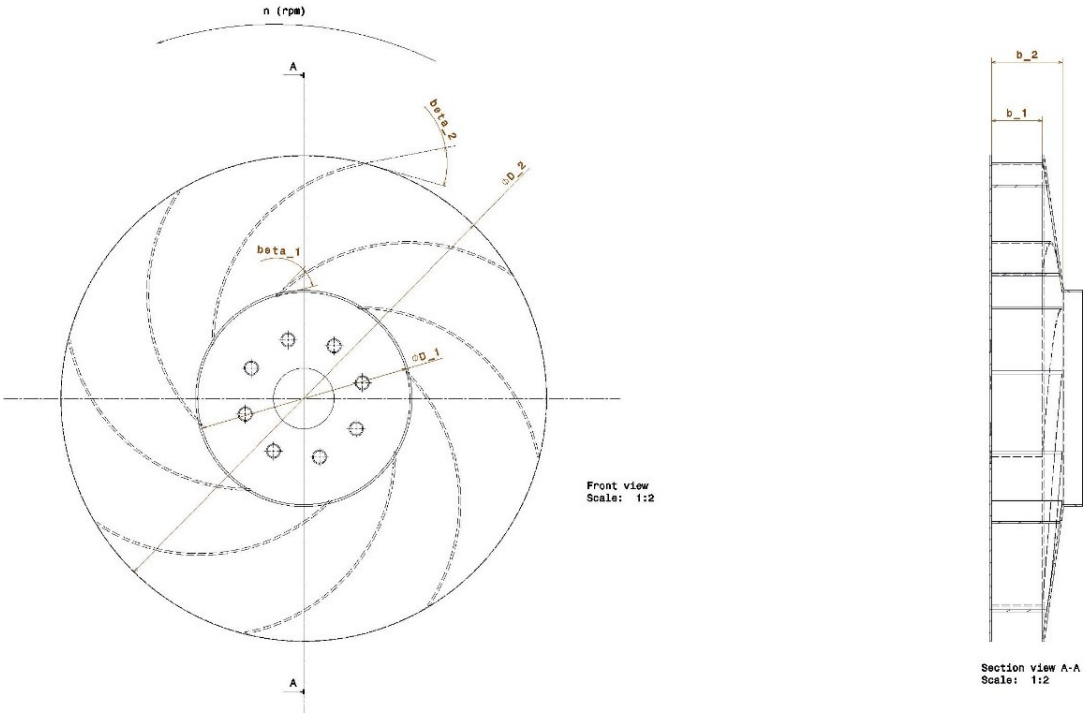

Figure 15: Back curved centrifugal impeller's mechanical drawing with front and side view. The design parameters are inserted in the dimensioning of each feature.

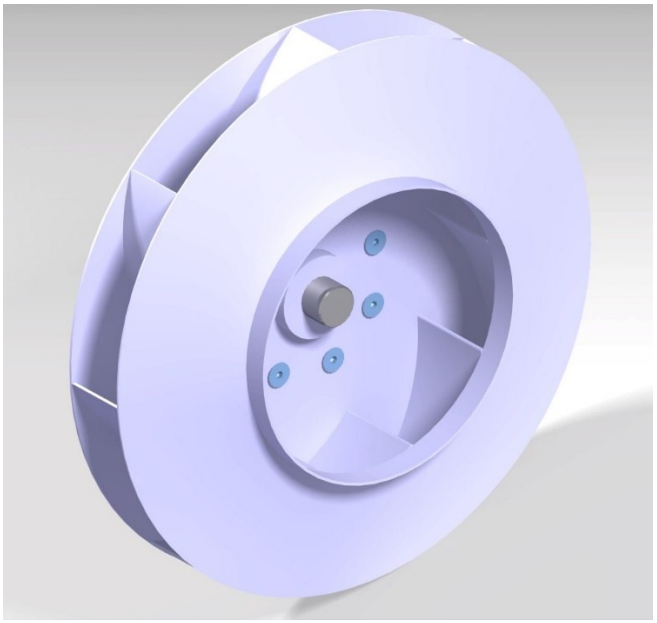

Figure 16: 3D model of the back curved centrifugal impeller.

For the cyclone, the following parameters had to be selected:

- Top cone's length L_u
- Cylindrical barrel diameter D_B and length L_B
- Lower cone length L_d and diameter D_d
- Inlet pipe's length (for the impeller) L_i
- Inlet hose z-coordinate z_H

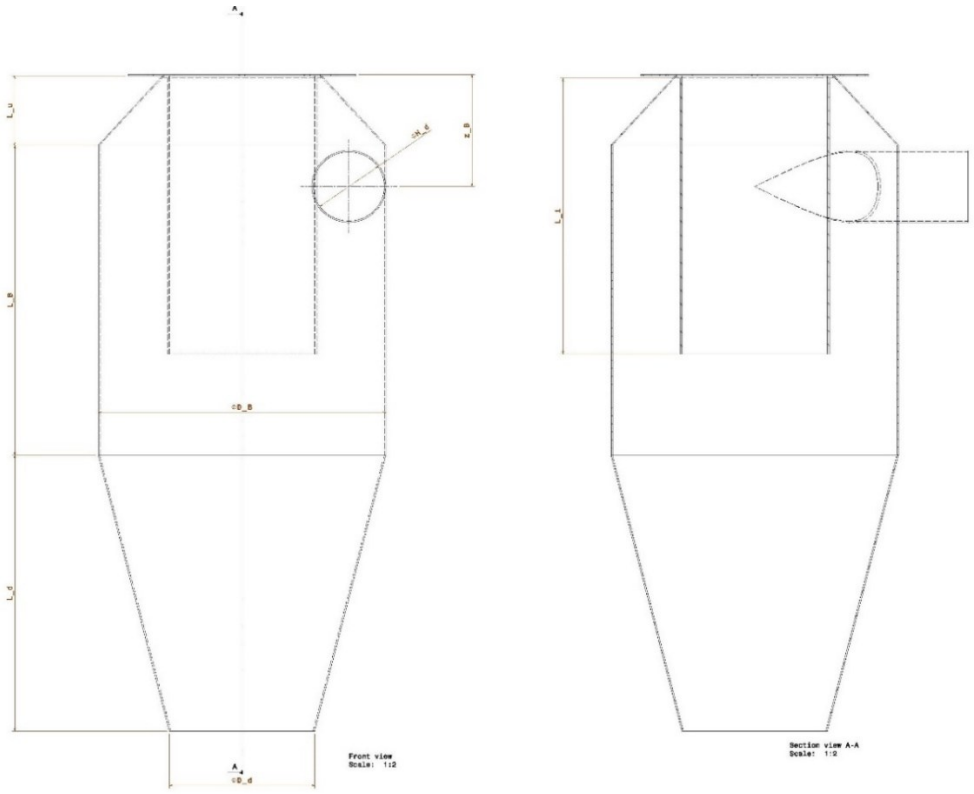

Figure 17: Cyclone's mechanical drawing with front and section views. The design parameters are inserted in the dimensioning of each feature.

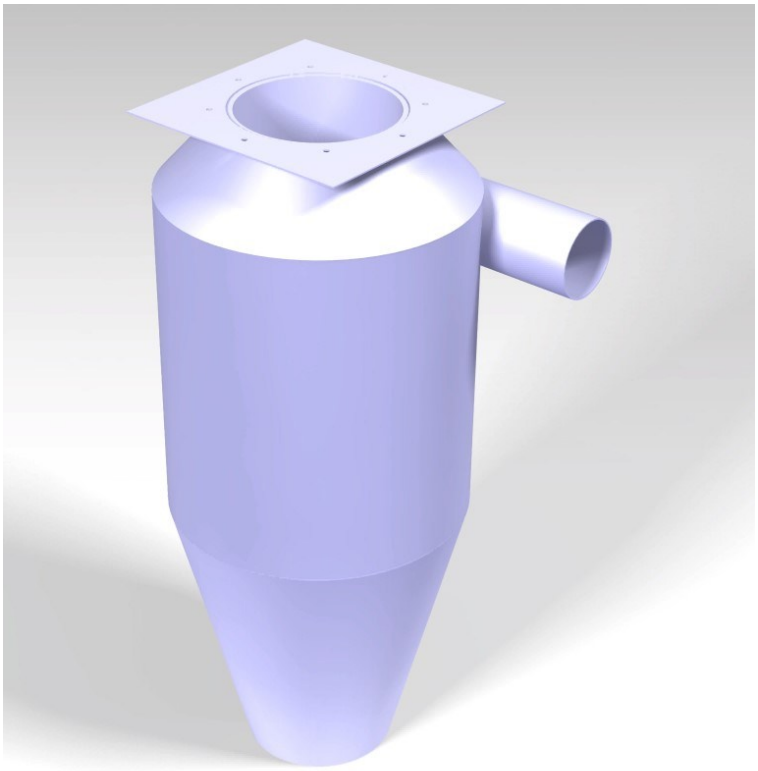

Figure 18: 3D model of the cyclone, designed in a CAD software.

The initial attempt at parameter selection for each component posed a significant challenge, primarily because all components collectively interact in numerous complex phenomena. In more detail, the impeller imparts flow and pressure to the air in accordance with its characteristic curve and the corresponding system curve. Hence, the impeller's parameters alone cannot determine the desired operating point, because the impeller's parameters influence only the impeller's characteristic curve. Unfortunately, the impellers parameters alone cannot reproduce the impeller's characteristic curve, because when the flow is induced, unpredicted phenomena take place inside the impeller's fan and casing, such as secondary flows and flow separation from the impeller's blade. These phenomena are identified accurately only through experimental measurements.

Furthermore, there are no available bibliographic evidence regarding the aerodynamic properties of olive fruit particles. The optimization of the aspirator device configuration primarily relies on experimental data from previous attempts, which can be manipulated using similarity laws. Additionally, this experimental data can be used for determining the friction factor and the aerodynamic drag of the material being conveyed.

Due to the absence of experimental data, the only viable solution was to employ reverse engineering for the parameter's selection, especially for the case of the cyclone. Regrettably, the author did not have any cyclone component for physical examination, so the reverse engineering process was executed by examining images sourced from the internet. The examination entailed analysing images that featured the cyclone component alongside objects of known dimensions. By employing similarity ratios, the dimensions of the cyclone were extracted through this process.

Figure 19: Aspirator device with cyclone. [Source: crfcostruzioni.it]

Selecting the parameters for the impeller presents a more intricate challenge, as there is no easy way to find images for the specific impeller used in an aspirator device. Furthermore, designing an impeller from the ground up becomes an insurmountable task when the required flow and pressure are not pre-defined. The most practical and feasible solution is to set some upper and lower limits by applying a theoretical analysis. The lower limit for the necessary air flow rate can be set by calculating the saltation velocity. Then, an upper limit can be set by applying the air-speed triangles in different sets of impeller design parameters and calculate the theoretical flow and theoretical pressure gain. Then, using the calculated theoretical flow, along with some assumptions for the solid particles flow, an initial estimate can be gained for the system's pressure losses. Unfortunately, the above process includes a lot of assumptions, but it can serve as a starting point for the first design, as it has the potential of delivering results that might share an order of magnitude for some quantities close to the actual case and even indicate infeasible sets of design parameters.

3.2. Saltation velocity calculation

As mentioned in chapter *2.3*, the saltation velocity is the threshold value that distinguishes the dilute-phase regime from the dense-phase. Hence, the saltation velocity is a lower bound for the velocity of the air stream when the airflow is in the hose. Consequently, an effort was made to estimate the saltation velocity. Lots of empirical formulas for the estimation of the saltation velocity can be found in the bibliography, some of them are listed in the following table.

Table 2: Saltation velocity empirical formulas [3]

Equations for saltation velocity	Author
$\mu = \frac{1}{10^{\delta}}\left(\frac{v_s}{\sqrt{gD}}\right)^{\chi}$, *where* $\delta = 1.44d + 1.96$ *and* $\chi = 1.1d + 2.5$ (3.1)	Rizk
$\mu = \alpha\left(\frac{\rho_b}{\rho}\right)^{a}\left[\frac{w_{f0}}{10(gD)^{0.5}}\right]^{b}\left[\frac{v_s}{10(gD)^{0.5}}\right]^{c}$ (3.2) *where* $\alpha = 1.11\ a = 0.55\ b = -2.3\ c = 3.0$	Matsumoto
$\frac{d^*}{D} = 1.39\left(\frac{\rho_b}{\rho}\right)^{-0,74}$, *where* d^* *defines the critical diameter for coarse and fine particles.* $\mu = \begin{cases} 5.56 * 10^3\left(\frac{d}{D}\right)^{1.43}\left(\frac{Fr_s}{10}\right)^{4} & if\ d < d^* \\ 0.373\left(\frac{\rho_p}{\rho}\right)^{1,06}\left(\frac{Fr_p}{10}\right)^{-3.7}\left(\frac{Fr_s}{10}\right)^{3.61} & if\ d > d^* \end{cases}$ (3.3)	Matsumoto, two-equation method

To apply the above formulas for the calculation of the saltation velocity v_s, some parameters must be predetermined. The parameter d represents the particles diameter. Since the olive fruit particle is non-spherical, the equivalent diameter value will be used. The parameter D represents the piping's system diameter and in the case of the aspirator device it corresponds to the inlet hose diameter. Fortunately, this is a value that can easily be obtained from the existing commercial machinery of the aspirator device, since it is the only characteristic property that the manufactures provide when purchasing the product. Typical values for the inlet hose diameter vary within the range of $100mm$ to $140mm$. So, the value of the inlet hose diameter is selected to be $D = 120mm$.

The parameter μ stands for the mass load ratio, hence:

$$\mu = \frac{\dot{m}_s}{\dot{m}_f} \tag{3.4}$$

The determination of the mass load ratio parameter is a more intricate task, primarily because the aspirator device does not operate in conjunction with a feeding regulating component (feeder). Instead, the flow of solid material is interrelated with the airflow. To proceed with the attempt to calculate the saltation velocity this parameter must be set. According to bibliography, dilute phase conveying is achieved when the mass load ration μ, is below the value of 15. A preferred value according to research for dilute phase conveying state that the ratio solid to air is $2:1$ [4]. The solid mass flow of the aspirator device can be set as desired and after the operation it can be revised. For a satisfactory operation and for the aspirator device to make an improvement of the process of collecting the olive fruits it should operate around $60\ kg$ of olive fruits per minute, meaning a mass flow rate of $\dot{m}_s = 1\ kg/s$. Having set the mass load ratio, the solid mass flow and the diameter of the hose, the value of the air velocity can be determined.

$$v = \frac{\dot{m}_f}{\rho A} = \frac{\frac{\dot{m}_s}{\mu}}{\rho\left(\frac{\pi D^2}{4}\right)} = \frac{\frac{1}{2}}{1.184\left(\frac{\pi * 0.12^2}{4}\right)} = 37.34\frac{m}{s} \tag{3.5}$$

The values for the air's physical properties, like density and viscosity will be corresponding to temperature of 20^0C, hence:

$$\rho = 1.184\ kg/m^3 \text{ and } \eta = 1.87 * 10^{-5}\ kg * s^{-1} * m^{-1}$$

From the three empirical formulas the last two seem more reliable since they incorporate more data regarding the nature of the particles being conveyed, as they include the terminal (free fall) velocity w_{f0} and the particle's density ρ_p. Therefore, the particle's terminal velocity must be determined.

The bibliography has some empirical formulas for the determination of the terminal velocity and the drag coefficient, but the selection of the formula relies on the flow regime of the particle. To determine the flow regime, the Reynolds number of the particle Re_p, must be calculated.

$$Re_p = \frac{\rho v d}{\eta} = \frac{1.184 * 37.34 * 0.014}{1.87 * 10^{-5}} = 3.34 * 10^4 \tag{3.6}$$

Since the particle's Reynolds number lies in the range, $500 < Re_p < 2 * 10^5$, Newton's regime is applicable. So, for the drag coefficient the following convenient formula arises, which is convenient because it does not rely on unknown parameters.

Table 3:Aerodynamic drag coefficient in correlation with the particles Reynolds number

Flow regime	$\boldsymbol{Re_p}$	$\boldsymbol{C_D}$
Newton's range	$500 < Re_p < 2 * 10^5$	0.44

The terminal velocity in the Newton's range for spherical particles is given from the following formula:

$$w_{f0} = \left(\frac{4}{3}\frac{d}{C_D}\frac{(\rho_b - \rho)}{\rho}g\right)^{0.5} \tag{3.7}$$

and for a non-spherical particle:

$$\frac{(w_{f0})_\psi}{(w_{f0})_1} = 0.843\log\left(\frac{\psi}{0.065}\right) \tag{3.8}$$

So,

$$w_{f0} = \left(\frac{4}{3}\frac{0.014 * (1042.16 - 1.184)}{0.44 * 1.184} * 9.81\right)^{0.5} = 19.2\frac{m}{s}\ ,\ (w_{f0})_\psi = 18.9\frac{m}{s}$$

All the parameters needed for applying the saltation velocity's formulas have been calculated or estimated, so substituting the values of the parameters and solving for the saltation velocity, gives:

1. Risk equation:

$$\delta = 1.44d + 1.96 = 1.44 * 0.014 + 1.96 = 1.98$$

$$\mu = \frac{1}{10^\delta}\left(\frac{v_s}{\sqrt{gD}}\right)^\chi \rightarrow v_s = (\mu * 10^\delta)^{\frac{1}{\chi}} * \sqrt{gD} \rightarrow v_s = (2 * 10^{1.92})^{\frac{1}{2.515}}\sqrt{9.81 * 0.12}$$

$$v_s = 8.76\ m/s$$

2. Matsumoto equation:

$$\mu = \alpha\left(\frac{\rho_b}{\rho}\right)^a\left[\frac{w_{f0}}{10(gD)^{0.5}}\right]^b\left[\frac{v_s}{10(gD)^{0.5}}\right]^c$$

$$v_s = \left(\frac{1}{a}\mu\left(\frac{\rho_b}{\rho}\right)^{-\alpha}\left[\frac{w_{f0}}{10(gD)^{0.5}}\right]^{-b}\right)^{\frac{1}{c}} 10(gD)^{0.5}$$

$$v_s = \left(\frac{1}{1.11}2\left(\frac{1042.16}{1.184}\right)^{-0.55}\left[\frac{19.2}{10(9.81 * 0.12)^{0.5}}\right]^{2.3}\right)^{\frac{1}{3}} 10(9.81 * 0.12)^{0.5}$$

$$v_s = 5.9\ m/s$$

3. Matsumoto two-equation:

$$\frac{d^*}{D} = 1.39\left(\frac{\rho_b}{\rho}\right)^{-0,74} \rightarrow d^* = 1.39D\left(\frac{\rho_b}{\rho}\right)^{-0,74} \rightarrow d^* = 1.39 * 0.12\left(\frac{1042.16}{1.842}\right)^{-0,74} \rightarrow d^* = 0.921\ mm$$

The olive fruit equivalent diameter is $d = 14.1\ mm$. Since $d > d^*$, the second equation for coarse particles will be used.

$$\mu = 0.373\left(\frac{\rho_p}{\rho}\right)^{1,06}\left(\frac{Fr_p}{10}\right)^{-3.7}\left(\frac{Fr_s}{10}\right)^{3.61}$$

where $Fr_p = \frac{w_{f0}}{\sqrt{gd}} = \frac{19.2}{\sqrt{9.81*0.014}} = 51.59$

$$Fr_s = 10\left(\frac{1}{0.373}\mu\left(\frac{\rho_p}{\rho}\right)^{-1,06}\left(\frac{Fr_p}{10}\right)^{3.7}\right)^{\frac{1}{3.61}}$$

$$Fr_s = 10\left(\frac{1}{0.373}2\left(\frac{1042.16}{1.842}\right)^{-1,06}\left(\frac{51.59}{10}\right)^{3.7}\right)^{\frac{1}{3.61}}$$

$$Fr_s = 11.69$$

where $Fr_s = \frac{v_s}{\sqrt{gD}}$

$$v_s = Fr_s\sqrt{gD} \rightarrow v_s = 11.69\sqrt{9.81 * 0.12}$$

$$v_s = 12.68\ m/s$$

The results from all the empirical equations for the saltation velocity are listed in the following table for the reader to easily see.

Table 4: Numerical results of the saltation velocity value for each equation of Table 2.

Saltation velocity v_s	Author
$\mathbf{8.76\ m/s}$	Rizk
$\mathbf{5.9\ m/s}$	Matsumoto
$\mathbf{12.68\ m/s}$	Matsumoto two-equations

As a precautionary measure and considering that the Matsumoto two-equations method incorporates a more comprehensive dataset regarding particle properties, the result of the third equation $v_s = 12.68\ m/s$ will be selected. Also, all those empirical formulas experience deviations close to 60%, according to the bibliography, therefore a safety factor of 2 will be considered.

From the above analysis, the impeller that will be selected has to deliver an air flow velocity of $v = 25\ m/s$, when a hose with diameter $D = 120\ mm$ is used. Although this value does not correspond to the free-air delivery, but rather the air stream velocity when the system is also loaded with solid particles. So, the free air flow delivery of the fan should be greater than:

$$Q = vA = v\pi\left(\frac{D}{2}\right)^2 = \pi * 25 * \left(\frac{0,12}{2}\right)^2 = 0.283\frac{m^3}{s} \quad (3.9)$$

3.3. Centrifugal fan's design parameters

A typical centrifugal fan characteristic curve is flat compared to other types of prime movers, meaning that a significant change in the air stream velocity will result in a small change in the pressure drop. The insertion of solid particles in the system will induce an additional pressure drop, so the operation point will have a smaller air stream velocity compared to the free air delivery system. Hence, when measuring the impeller's flow in free delivery with a hose diameter of $D = 120\ mm$, a speed greater that $v = 25\ m/s$, must be achieved (air flow $Q = 0.28\ m^3/s$).

The best choice available to the author was to use the formulas presented in chapter 2.1 about the relationship between the impeller design parameters with the induced flow and head induced by the impeller. It is important to note that those formulas will give a set of (H, Q) values that correspond to the optimum working point of the impeller, not the actual operation point of the whole piping system, since in a stable steady state, the head H, will match the system's needs for pressure drop. Furthermore, this type of analysis does not consider the hydraulic and friction losses inside the impeller.

The approach for conducting the impeller's analysis was to fill out a set of values for the design parameters and observe the output values, repeating this process until a set of output values has the desired quantity. The desired quantity is defined by a flow greater than $Q = 0.28\ m^3/s$ and a power consumption around $4\ kW$, as this will be roughly the order of magnitude of the power unit. The starting point of the input set had values outer diameter around $D_2 = 400\ mm$ and blade width around $b = 50\ mm$ as those values were observed by the author in some back-curved centrifugal impellers.

The following figure presents the calculation sheet that holds the final iteration and displays the selected design parameters with the corresponding theoretical flow Q_u and the theoretical power of the impeller.

$$c_{r2} = \frac{Q_u}{(\pi D_2 - Z_B s_2) b_2} \qquad Q_u = u_1 \tan(\beta_1) * (\pi D_1 - Z_B s_1) b_1$$

$$c_{u2\infty} = u_2 - \frac{c_{r2}}{\tan \beta_2}$$

n(rpm)	D1 (mm)	u1(m/s)	b1(mm)	β1(degrees)
2800	200		70	30
ω(rad/s)	D1 (m)	29.3215	b1(m)	tan(β1)
293.215	0.2		0.07	0.5774

D2 (mm)	u2(m/s)	b2(mm)	β_2,B(degrees)
490		40	25
D2 (m)	71.8378	b1(m)	tan(β2)
0.49		0.04	0.4663

Optimum working point	
c_r1 (m/s)	16.93
c_r2 (m/s)	11.92
Q_u,A (m^3/s)	0.72
Q_u,A (L/s)	716.13
c_u2,ideal (m/s)	46.27
N_ideal (W)	2818.22
H_u,ideal (mY)	338.82

$$Power = \Delta p * Q = \rho g\, H\, Q$$

$$w_{s2} = x * u_2$$

$$c_{u2} = c_{u2,\infty} - w_{s2}$$

Theoretical quantities	
w_s2 (m)	11.85
c_u2 (m/s)	34.42
H_u (mY)	252.06
η_ideal	0.74
N_theor (W)	3788.19

Slip Factor x

e1(mm)	1.5	e2(mm)	2	Pfleideler	
Zβ	8			k	x
s1(m)	0.003	s2(m)	0.00473	0.8536	0.1649

$$x = 2k \frac{gH_{u,i}}{u_2^2} \frac{1}{Z_B \left[1 - \left(\frac{D_1}{D_2}\right)^2\right]} \qquad where\ \ k = 0.6[1 + \sin(\beta_2)]$$

Figure 20: Calculation of flow Q and Power consumption N using the theoretical air velocity triangles at the optimum working point for a given set of design parameters.

The iterative process stopped, since a theoretical power close to the desired value was achieved and theoretical flow $\frac{0.72}{0.28} = 2.5$ times bigger than the limit that corresponds to the saltation velocity. As

seen in the calculation sheet the radial impeller has variance to its width (conical design) as this practice was observed by the author in other designs. Furthermore, the rmp value was selected having in mind the typical values that the tractor will feed the hydraulic motor (this is the typical power unit used in the causes of machinery that its power is fed through a tractor). The $Pfleideler$ semi-empirical formula was used to calculate the slip factor x, used to convert the ideal speed triangle to the theoretical speed triangles.

An important note is that one of the reasons that the iterative process ended when the resulted flow was 2.5 times higher than the flow needed for the saltation threshold is that, besides the fact that a operational point near the threshold is not desired, and the fact that the theoretical flow does not take into account the hydraulic losses due to recirculation of the flow that happens inside the impeller. This is also the case for the theoretical head, as friction losses take place inside the impeller.

Table 5: Centrifugal fan's parameters

Parameter's description	**Parameter's value**
Inlet diameter $\mathbf{D_1}$	$200\ mm$
inlet blade width b_1	$70\ mm$
Outlet diameter D_2	$490\ mm$
outlet blade width b_2	$40\ mm$
Blade's leading-edge angle β_1	30^0
Blade's trailing-edge angle β_2	25^0
Rotational speed n	$2800\ rpm$

The design of the centrifugal impeller was executed using CAD software, before the actual construction, for the purposes of representation and prototyping. Furthermore, this approach enabled the assessment of dimensional consistency among components, with the goal of identifying and rectifying any errors in component dimensions that might affect their compatibility with the impeller. To ensure design flexibility and the adaptability of the design to various setups, the CAD design of the impeller adheres to a parametric paradigm. The blade shape of the impeller was selected to be a straightforward circular arc. This choice was made due to its prevalence in designs and its ease of construction.

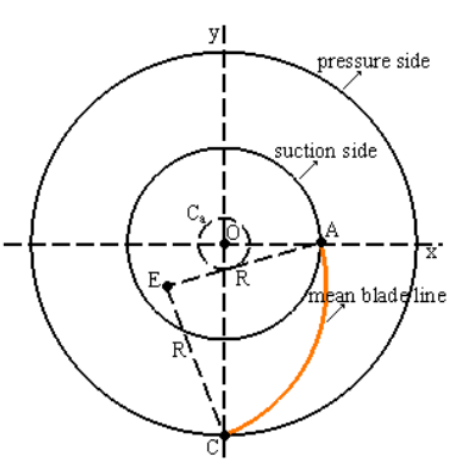

Figure 21: Method for implementing a parametric design of the blade of a centrifugal impeller. [Source: "Parametric study performance of a centrifugal pump based on simple and double arc design methods"] [7]

The parametric design of the impeller's blade required a further investigation as the blade $2D$ profile doesn't have a fixed start and end point due to the inlet and outlet diameter variation, nor a fixed angles at the trailing and leading edge. The method that was followed is described in *Figure* 21, according to [7].

It is worth mentioning that the author undertook the effort to calculate the $pressure\ losses$ of the piping system, given the calculated theoretical flow of the impeller, that was derived from the iterative process of the impeller calculation sheet (*Figure* 20). As described in chapter 2.4, the system pressure losses depend on quantities that are not determined before the operation, as well as quantities that require experimental measuring; so, the evaluation of the $Power$ equation is not feasible from the system's perspective. Nevertheless, the endeavor of calculating some contributions of pressure losses could give an initial estimate on whether the induced flow and head from the impeller is even feasible at the given conveying system. Before commencing the effort to calculate certain contributions to the system's pressure losses, the following paragraph explains in more detail the reasons that the calculation of the system pressure losses cannot be carried out in an accurate manner.

As mentioned in the section *2.4*, the pressure drop regarding the solid particles flow requires the knowledge of the particle's velocity c, for calculation of the solid friction factor λ_Z, the pressure drop due to acceleration of the solid particles and the pressure loss due to vertical elevation. The particle's velocity is a parameter that cannot be estimated, even if the solid mass flow rate is measured, since it is a function not only of the mass flow rate but also of the voidage. The relation between the particle's velocity c, the solid mass flow rate $\dot{m}_s$ and the voidage ε, is shown below. The definition of the voidage ε, is described in the following paragraph with the help of *Figure* 22.

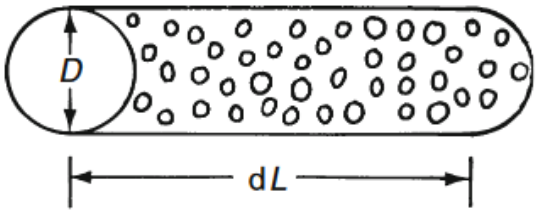

Figure 22: Volume element of the piping system with solids flow inside the pipe. [Source: "Pneumatic conveying of solids"] [1]

As shown in the figure above, the solid's flow is not extended to the entire cross-sectional area of the pipe, but rather to a percentage. The percentage of the solid's volume relative to the entire volume of a volume element of the piping system is represented by the voidage ε, so:

$$\varepsilon = 1 - \frac{V_s}{V} \tag{3.9}$$

Hence the solid mass flow ratio is given from the following formula.

$$\dot{m}_s = \rho_p(1-\varepsilon)Ac \tag{3.10}$$

Another parameter that remains undetermined is the solid effect friction factor λ_Z^* (as shown in Equation 2.8). This parameter has a similar nature as the $Darcy\ friction\ factor\ f_D$, as it depends not only on the properties of the conveyed material but also on the state of the conveying system. For example, bibliography includes plots of experimental data that relate λ_Z^* with the mass load ratio μ under a given set of material and pipe properties. The reason for the dependance in the mass load ratio comes from the fact that the friction and impact forces cannot be modeled separately.

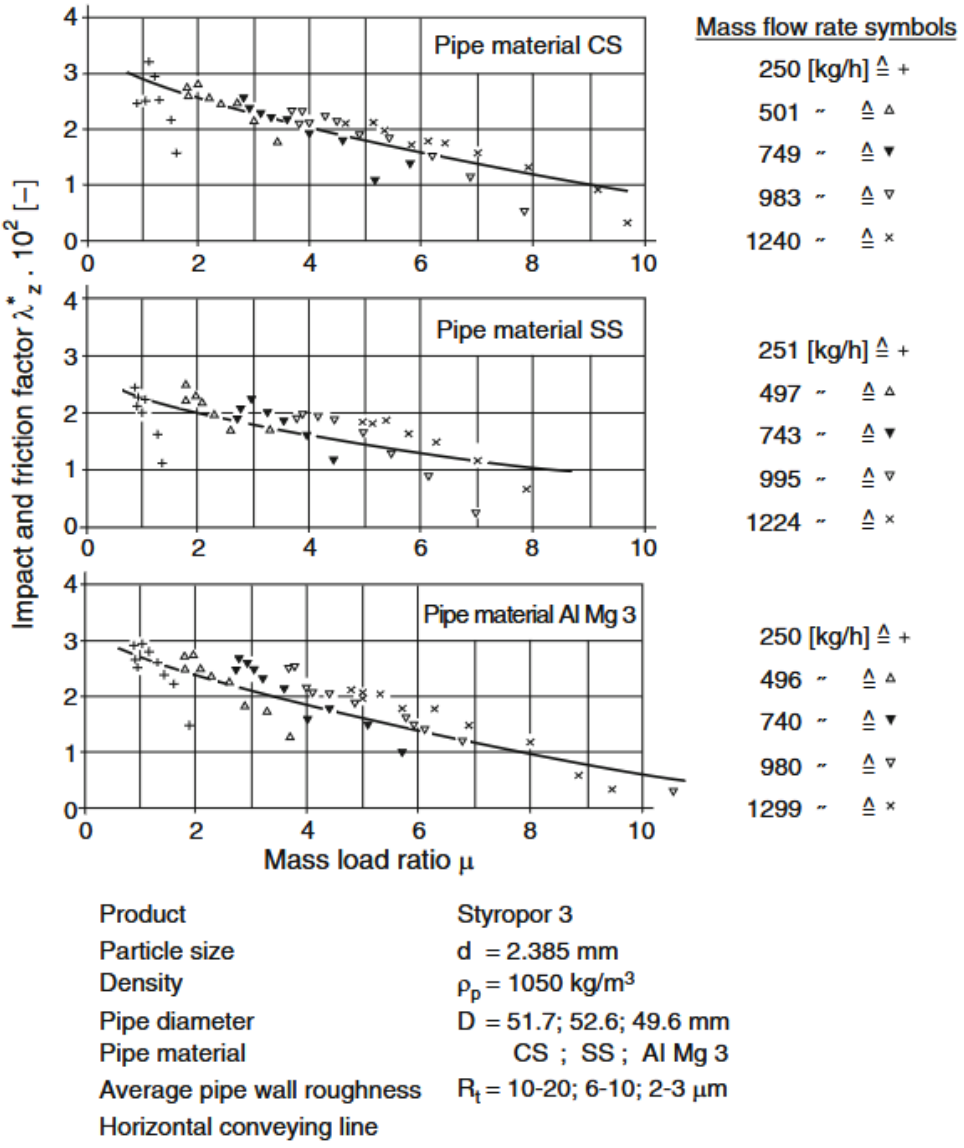

Figure 23: Experimental data the correlates the impact and friction factor with the mass load ratio, under a specific set of material and piping properties. [3]

The above figure indicates that the values of the impact and friction factor λ_Z^* cannot be used for the conveying system of the olive fruits that is under investigation in the current paper. Nevertheless, an insight in the order of magnitude of the factor λ_Z^* can be obtained.

Furthermore, the presence of a cyclone geometry induces complex flow patterns, as presented in the next chapter, that are hard to model in terms of pressure loss.

3.4. Estimation of system pressure loss

Having cleared out the capabilities and purpose of the endeavor to calculate the system's pressure losses, it is time to use the formulas mentioned in 2.4 in combination with some empirical formulas and some assumed values, within an reasonable order of magnitude, to get and estimation of whether the system pressure loss is overcoming the available pressure gain of the impeller at the calculated flow (from *Figure 20*).

Air Density (kg/m^3)	1.184
density (kgr/m3)	1042.16
air viscocity μ	1.85E-05
g(m/s^2)	9.81
Q_u (theoretical flow) [m^3/s]	0.72
η_Q (hydraulic coef)	0.9
Q (flow) [m^3/s]	0.648
Hose Diameter (m)	0.12
Air Hose Speed (m/s)	57.296
particle diameter(m)	0.014
plastic hose roughness	5.00E-04
relative (e/D)	4.17E-03
Reynolds	4.40E+05
f_D (Moody)	0.0288
μ (solid mass ratio)	0.5
w_f (m/s)	18.9
Dean number_1	7.02E+03
Dean number_2	4.63E+04
Dean number_3	2.80E+02

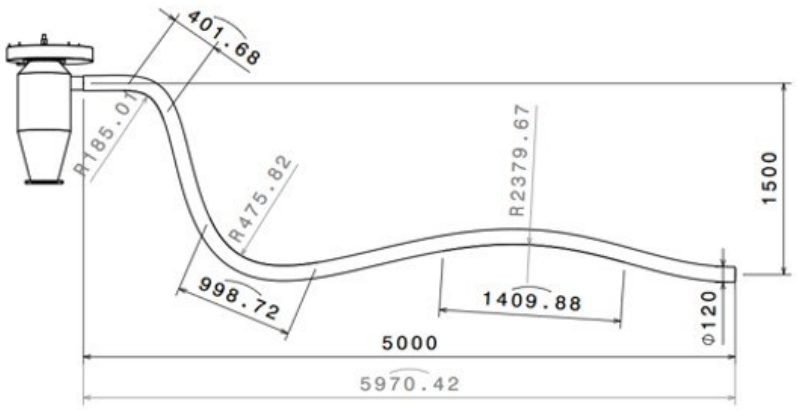

$$\Delta p_{bend} = \frac{0.029 + 0.304\left[Re\left(\frac{D}{2R_b}\right)^2\right]^{-0.25}}{\left(\frac{2R_b}{D}\right)^{\frac{1}{2}}} \frac{L_b \rho v^2}{2D}$$

System pressure losses

Linear air losses

Length (m)	f_D	Δp_linear (Pa)
5.97	0.0288	2.78E+03

$$\Delta p_l = f_D \frac{L}{D} \frac{\rho_{air} v^2}{2}$$

Vertical losses

h (m)	Δp_vertical (Pa)
1.5	1.74E+01

$$\lambda_z = \frac{c}{v}\lambda_z^* + 2\frac{v}{c}\frac{\beta}{Fr^2}$$

λ*_ζ	λ_ζ	β	c	Δp_solid_friction (Pa)
0.05	0.01019	1	6.212601976	4.93E+02

$$\Delta p_z = \mu \lambda_z \frac{\rho v^2}{2} \frac{\Delta L}{D}$$

Solid Bend losses

L_b	R_b (m)	Δp_bend_solid
0.401	0.475	1.44E+02
0.998	0.185	5.73E+02
1.409	2.379	2.25E+02

Solid Verical losses

Δp_solid_Height (Pa)
8.03E+01

$$\Delta p_{height} = \mu\, \rho\, g\, H \frac{v}{c}$$

Acceler losses

Δp_acc (Pa)
2.11E+02

$$\Delta p_{accelaration} = \mu \rho c v$$

Fr_p	Fr	c/v
50.82	62.17	0.1084

$$\frac{c}{v} = \frac{1 - \sqrt{\frac{\lambda_Z^*}{2} Fr_p^2 \left(1 - \left(\frac{w_f}{v}\right)^3\right) + \left(\frac{w_f}{v}\right)^3}}{1 - \frac{\lambda_Z^*}{2} Fr_p^2}$$

Total losses

Δp (Pa)	Power (W)
4.53E+03	2.42E+03

Figure 24: System pressure loss calculation sheet.

The following formulas and assumptions were made to carry out the estimation of Δp_{system}.

1. Linear air losses were calculated by using (2.5). The f_D factor was retrieved from a Moody diagram and the air flow speed was retrieved from the hose diameter and the flow induced by the impeller as calculated in the impeller calculation sheet (*Figure* 20).
2. Vertical air losses were calculated by using formula $\Delta p_{hydrostatic} = \rho g h$
3. For the solid impact and friction losses:
   a. An arbitrary value for the λ_Z^* was selected in the order of magnitude that particles with approximate diameter and approximate mass load ratio.
   b. For the λ_Z calculation the solid particle's speed c must be calculated. Since no experimental data was available, the following empirical formula was used [3]:

$$\frac{c}{v} = \frac{1 - \sqrt{\frac{\lambda_Z^*}{2} Fr_p^2 \left(1 - \left(\frac{w_f}{v}\right)^3\right) + \left(\frac{w_f}{v}\right)^3}}{1 - \frac{\lambda_Z^*}{2} Fr_p^2}$$

The terminal velocity w_f value has already been calculated for the saltation velocity calculations (3.2).

c. The pressure losses that the solid particles induce due to the bends in the hose are calculated using (2.10) and the bends radius and lengths are derived from the hose modeling. This represents an approximation of the actual conditions, as the hose will undergo random motions in practice.
d. The value for the air stream flow is derived from the impeller calculation sheet (*Figure* 20), with a slight modification to reflect a more realistic scenario, as this flow rate is multiplied by a volumetric-efficiency factor $\eta_Q = 0.9$.

After aggregating all contributions to the pressure losses, the system pressure loss is equal to: $\Delta p_{system} = 4.53\ kPa$. After multiplying the pressure loss with the induced flow, the power consumption of the system is equal to $N_{system} = 2.42\ kW$

The above result is encouraging as it is less than the power calculated in the impeller calculation sheet (*Figure 20*) leaving a relatively high margin between the two values. This margin is particularly important, as the cyclone pressure loss was not included in the above calculation. Additionally, the results suggest that the impeller's high flow rate contributes significantly to the system's overall pressure loss.

3.5. Cyclone's design parameters

The cyclone's geometry induces a complex pressure drop that is difficult to predict. The cyclone's primary flow regime is centrifugal air flow, which results in high pressures along the outer wall region, while the core region remains at low pressures. This pressure differential generates a secondary flow along the walls of the lid with an inwards radial direction (1). Eventually, this flow derives a downward flow along the outer wall of the vortex finder (2). Just below the vortex finder, a radial inward flow creates a 'lip flow' (3), forming a flow channel that amplifies short-circuit and recirculation flows, as illustrated in the following *Figure 25*.

Furthermore, the cross section where the air and solids are separated cannot be accurately defined.

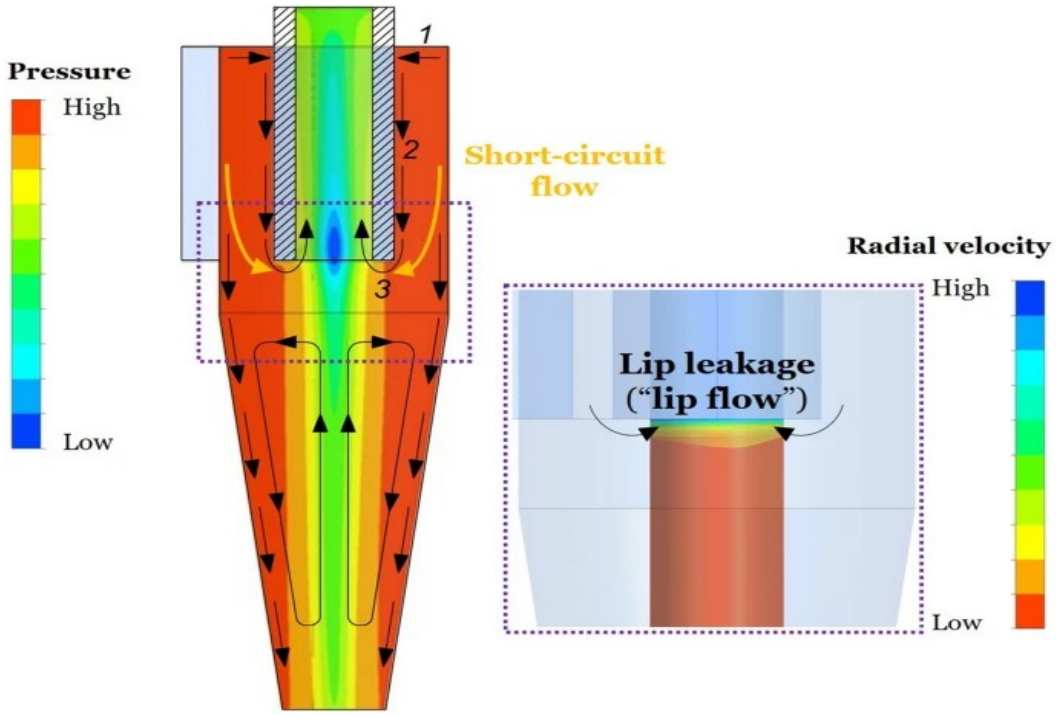

Figure 25: Air flow inside a cyclone. Several flow regimes can be found. 1: Inward radial flow. 2: Downward axial flow. 3: Lip flow with 180^0 turn. Also, a secondary turbulent flow can be seen. [Source: "Secondary Lip Flow in a Cyclone Separator"] [8]

As mentioned in section *3.1*, and considering the complexity that the cyclone's geometry induces to the system, the parameter selection of the cyclone was made from analyzing images of the cyclone's component used in commercial aspirator devices. The analysis of images was executed by comparing the pixels occupied of an object with known dimensions to the pixels occupied by the object that the dimensions wished to be acquired. For the cyclone, the dimensions of the inlet hose flange are known since the manufacturer is providing them. In the following image, the inlet hose flange has a diameter of $120mm$.

Figure 26: Pixel ratio of cyclone's parameters relative to the hose's inlet flange. [Source for image: "crfcostruzioni.it", source for image measurements:" https://eleif.net/photomeasure"]

In the above image the red line labeled with the index (1), corresponds to the reference pixel length. The rest of the green lines with indexes from (2) to (6), have a length unit that corresponds to a multiplier of the reference red line. Multiplying each green line's factor with the actual length in (mm), of the hose's inlet flange (red line), will result in the actual length of each component's dimension. Since the distance of each object from the camera is not known, the success of this process lies in the fact that the measured objects are approximately in the same plane. The results of the multiplications give the following table for the cyclone's design parameters.

Table 6: Cyclone design parameters.

Parameter's description	**Parameter's value**
Barrel's Diameter D_B	$400\ mm$
Barrel's Length L_B	$420\ mm$
Upper cone Length L_u	$120\ mm$
Down cone Length L_D	$300\ mm$
Down cone Diameter D_D	$180\ mm$
Hose inlet flange z-coordinate	$210\ mm$

Finally, a formation that is not visible from the images is the inlet pipe of the impeller (vortex finder). The purpose of that pipe is to make sure that the flow inside the cyclone is mainly centrifugal. This pipe begins at the impeller's inlet and extends downwards up to a certain height, probably lower than the hose's inlet flange height. Thus, it effectively mitigates the potential for a significant short-circuit flow, which might occur when air finds a direct path from the hose's inlet flange to the impeller's inlet. To address this issue, the author employed a practical solution by utilizing a single-stage telescopic pipe with an adjustable length and minimal reduction in cross-sectional area.

3.6. Operation of the cyclone aspirator device

After the operation of the cyclone's device different values for the length of the impeller's inlet pipe were tested. The findings revealed that positioning the pipe near the end of the barrel significantly reduced both the airflow and the solid mass flow rate. The sole positive outcome of extending the pipe's length (corresponding to a decrease in height) was an improvement in deleafing results.

Figure 27: Aspirator device with cyclone. The assembly of the device includes the hydraulic system for the impeller's rotation.

On the other hand, when the vertical position of the pipe was set to a high position, the free air flow increased and so did the solid mass flow, but the ability to expel leaves from the cyclone's hopper was reduced. Also, another downside was that the flow was more unstable, as it was observed that inside the cyclone the solid particles were sometimes not settling at the bottom of the hooper but rather they were suspended in a centrifugal flow. After conducting several experiments, an optimal hose position was identified, striking a balance between achieving satisfactory air and solid mass flow rates, effective leaves expulsion, and flow stability. In that setup the air speed was measured (when no solids particles were present, as the instrumentation would be damaged). Subsequently, the solid mass flow rate was determined by measuring the time required for a given mass of olive fruits to be conveyed.

Table 7: Air velocity solid mass flow data, obtained from the aspirator device operation.

Hose diameter D_{hose}	Impeller rotational speed n	Free air velocity v	$\dot{m}_{solid}$
$120\ mm$	$2800\ rpm$	$40\ m/s$	$20\ kg/min$

3.7. Manufacturing process of cyclone aspirator device components

3.7.1. Impeller's casing

The impeller casing plays a crucial role in fan efficiency, working in tandem with the impeller. Essentially, the casing functions as a vaneless diffuser, converting the kinetic energy of the air exiting the fan into static pressure.

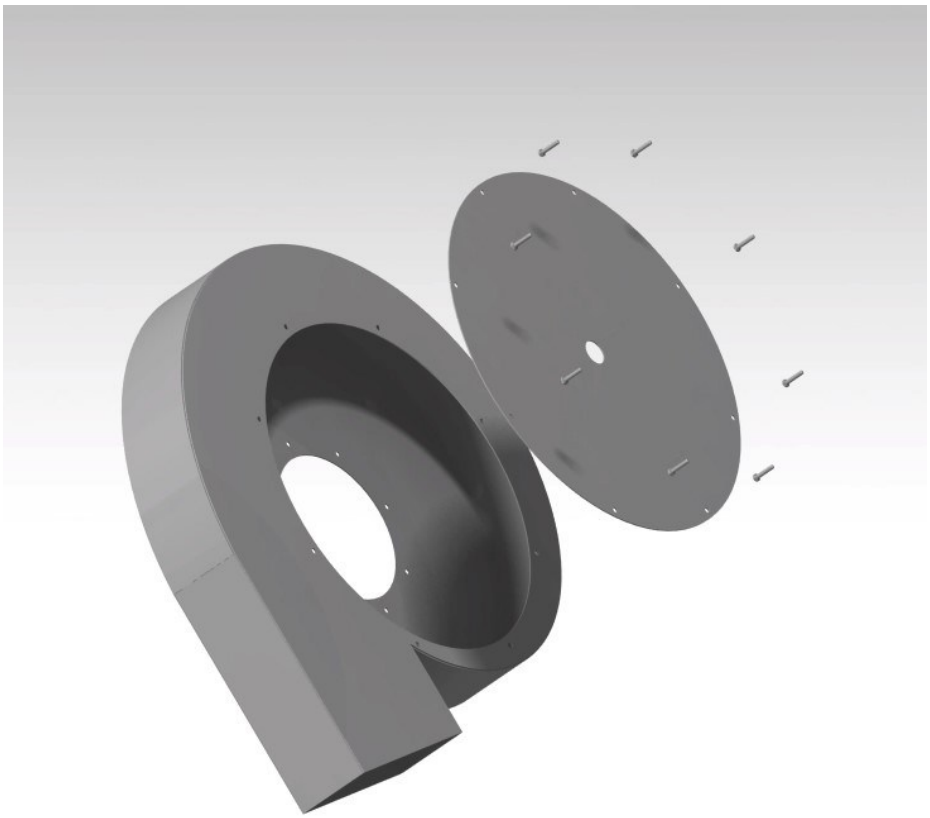

Figure 28: Impeller's casing. The plate and the flanges are welded, except the top plate that is assembled using bolts, for the impeller to be assembled inside the casing.

The manufacturing process of the casing commences with the cutting of the plate flange. The profile of the plate must follow a logarithmic spiral for the most efficient function of the radial diffuser. As the flow traverses the diffuser, due to continuity, the radial component of the air velocity decreases proportional to r. In addition, due to the angular momentum of the flow being conserved, the tangential component of the air velocity also decreases proportional to r. Therefore, the ratio of the radial to the tangential velocity is constant.

$$\frac{c_r}{c_u} = \tan(a_2) \tag{3.11}$$

where a_2 is the angle of the absolute velocity, relative to the tangential direction, of the air at the exit of the fan. The above condition determines the streamlines shape inside the casing as a logarithmic spiral; thus, the wall of the casing should have a matching profile to avoid disrupting the streamlined flow. Therefore, the function that defines the profile [12] is the following:

$$r(\theta) = R_2 \, e^{\theta \frac{Q}{2\pi B \, c_{u2} \, R_2}} \tag{3.12}$$

where B is the constant volute width and c_{u2} is the tangential air velocity at the exit of the impeller.

The relation (3.12), can be used for reproducing the profile of the logarithmic spiral in CAD software, as seen in *Figure 299*. The representation of the plate's profile in CAD software gives the possibility of exporting the design in $.dwg$ format, which can be fed to a CNC plasma cutter for an accurate formation of the desired complex shape.

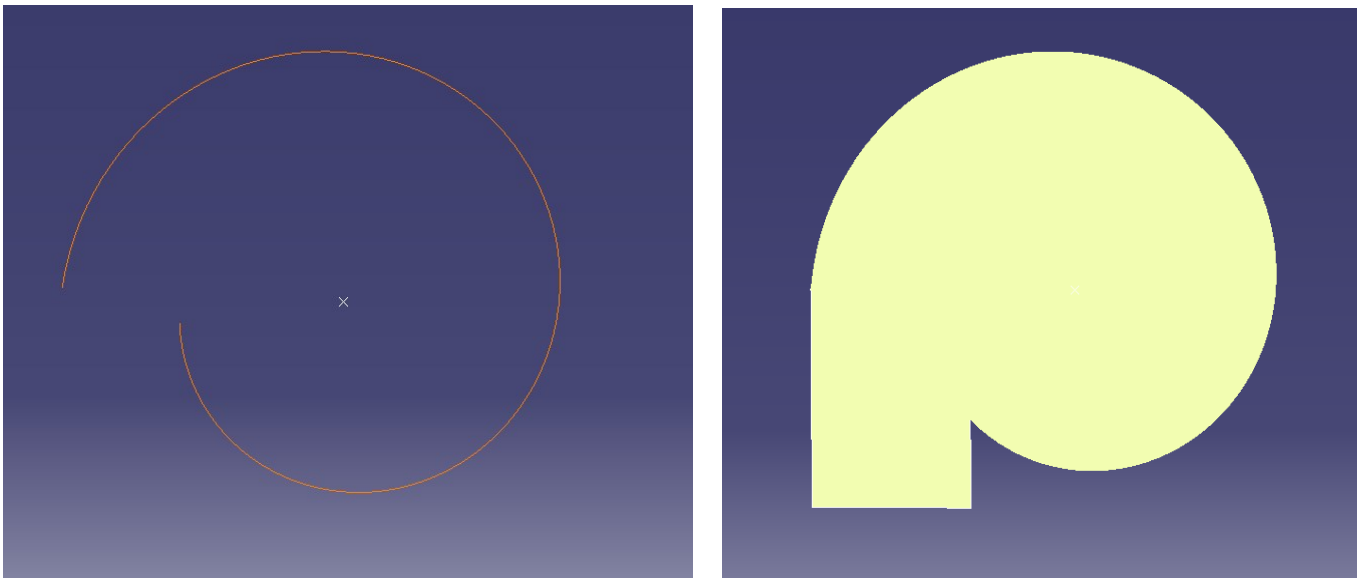

Figure 29: Logarithmic spiral curve (left image) and the surface profile of the plate of the casing (right image) designed in CAD software.

The above process was done to create the formations of both the back plate and the front plate of the casing. The front plate incorporates a hole for the impeller's air inlet, while the back plate features a large opening to facilitate the mounting of the fan inside the casing. Both plates are depicted in *Figure* 30*30*. The opening in the front plate is slightly larger compared to the fan's inlet diameter D_1, to allow the impeller's lip to pass through, creating a labyrinth-like effect. The opening at the back plate is slightly larger than the fan's diameter D_2, for the impeller to fit through when it is assembled or disassembled.

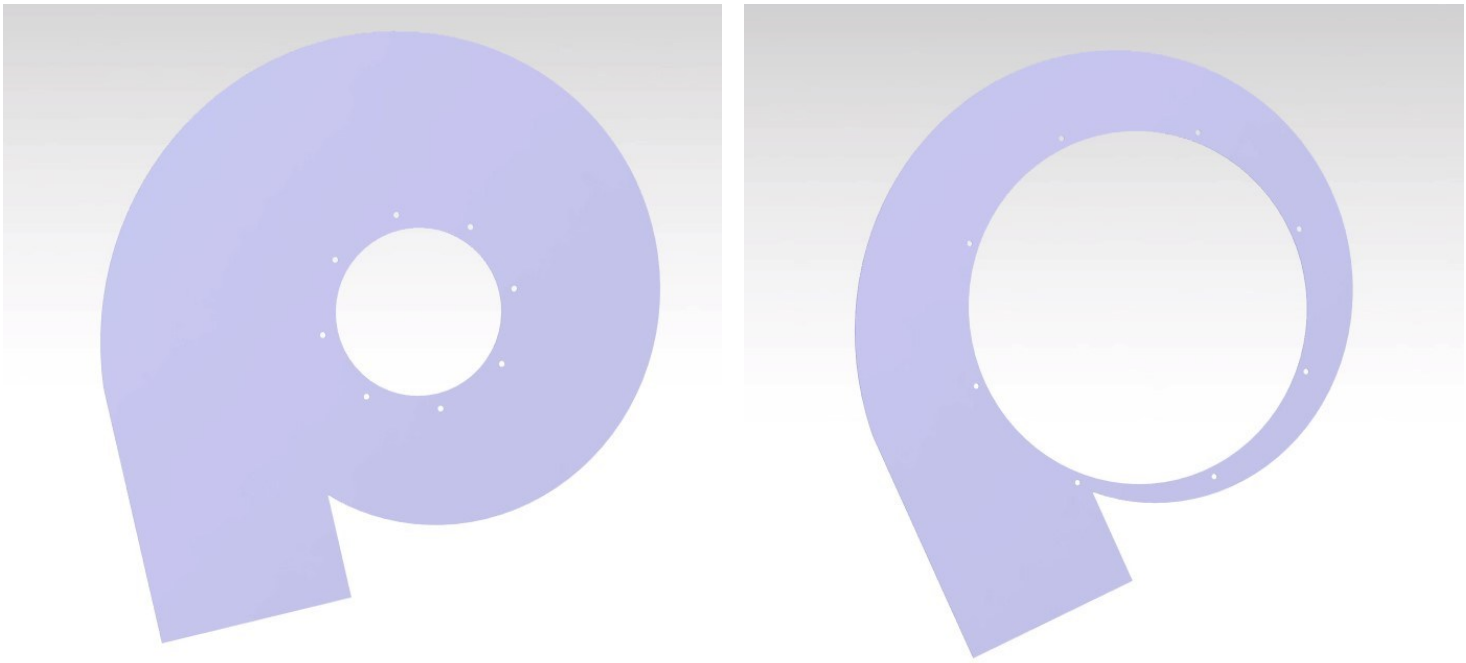

Figure 30: Casing's front plate with opening for the fan's inlet (left image). Casing's back plate with opening for the fan's assembly/disassembly (right image).

To create the entire casing assembly, a side flange was welded along the contour of the back plate flange, and subsequently, the front plate was welded on the opposite side of the side flange. The side flange was constructed using rectangular strips of steel plate. Initially, a sizable steel plate was gradually welded around the logarithmic spiral shape of the back plate. Following this, straight side flanges were welded to close the gaps at the exit formation. *Figure* 3131 provides an exploded view of all the flanges of the impeller's casing.

Figure 31: Exploded view of the impeller's casing. In this view all the individual flanges can be seen before welding together.

The tangible result of the casing manufacturing process, involving the shaping and welding of the flanges as described above, is depicted in the following *Figure* 32.

Figure 32: Result of manufacturing process of the impeller's casing.

After the description of the manufacturing process of the impeller's casing, it is important to note that the numerous parameters of the casing significantly impact the flow conditions and the impeller efficiency. Due to the complexity of modeling the parameters of the casing, the author adheres to the design parameters of casings that hold impellers of similar diameter D_2 and width b. The design parameters of the casing are illustrated in the following *Figure* 33.

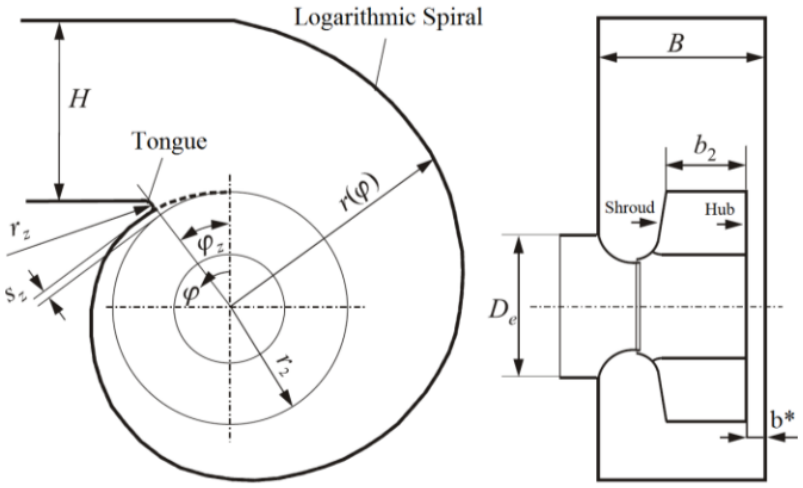

Figure 33: Impeller's casing design parameters. [Source: Effect of Clearance Gap in Spiral Casing Design of Centrifugal Fan with Optimized Impellers, Ardit Gjeta, 2019][11]

In more detail, the parameters that are shown in the previous figure is the width of the rectangular exit H, the height of the casing B, the tongue angle φ which is the angle that the side flange starts to form the logarithmic spiral, the radii r formed in the edge of the tongue for avoiding sharp edges and the clearance b^* between the fan's backplate and the casing bottom flange. All those values were selected by copying values of casings with similar impeller's dimensions and critical thinking.

3.7.2. Impeller's fan

The fan construction was done by welding the fan's blades to the back blade and then welding the conical shroud on the top side of the blades. The back plate was shaped by lathe-machining a circular steel plate to achieve a precise circular profile with a diameter of D_2. The blades were fabricated by cutting steel plates into a trapezoidal shape, with the two bases having dimensions equal to b_1 and b_2 respectively, while the height of the trapezoid was determined using the CAD representation of the impeller's fan. As mentioned in section *3.3*, a parametric design of the fan's blade was accomplished, allowing for the determination of the blade's trapezoid height based on the parameters outlined in *Table 5* and using the CAD utility of measuring the arc's length, as seen in the following *Figure 34*.

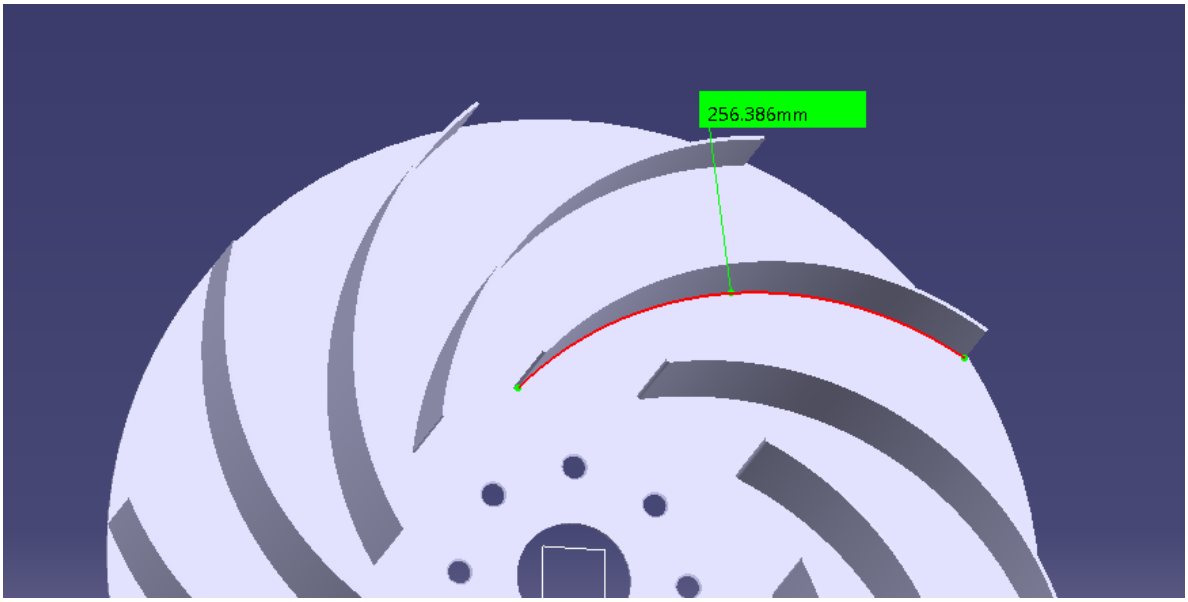

Figure 34: Measurement of the blades arc length in CAD software. This measurement was used for cutting the initial trapezoid steel plate from which the blade will be formed.

After the trapezoid steel plates were cut, using a roll plate bending machine, they were bent to a circular arc shape.

The shroud was formed by cutting a cone's layout from a steel plate and subsequently rolling the plate using a plate rolling machine. The two ends of the cone were welded together, and a lip formation was added at the top of the shroud. The lip serves a crucial role in guiding the airstream into the impeller's fan, eliminating sharp edges, and aiding in sealing the space between the inlet and the casing. This labyrinth-like effect increases the flow resistance of the path leading directly from the inlet to the casing, bypassing the impeller's fan. The three main components that were welded together to create the fan assembly are illustrated in *Figure* 35, in an exploded view.

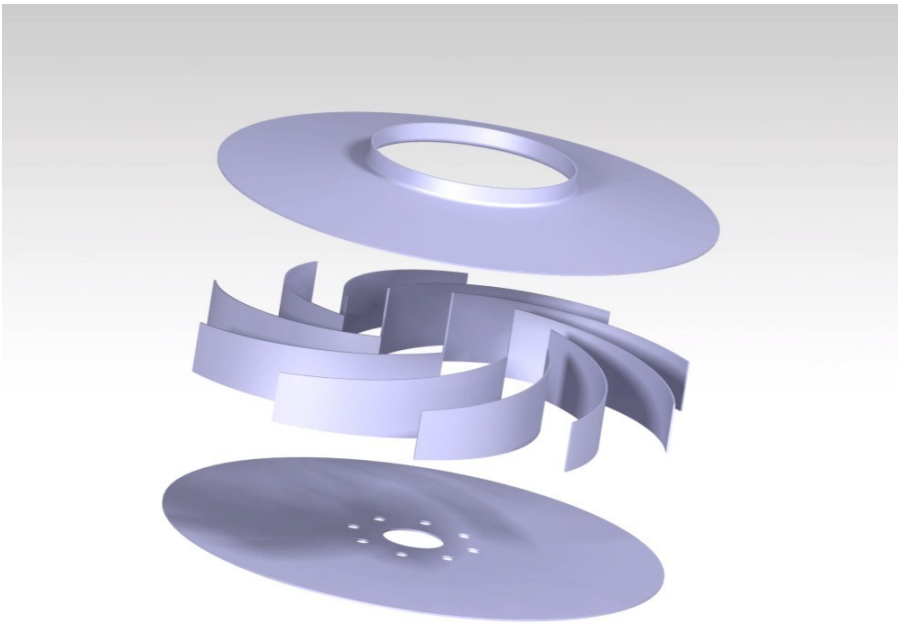

Figure 35: Exploded view of the centrifugal impeller. The back plate, the blades and the shroud were welded together forming the blower assembly.

To transmit power to the impeller and enable its rotation, the impeller must be connected to a shaft. The other end of the shaft is connected to the primary mover, which was selected to be a hydraulic motor. For proper function, especially in the stage of starting the impeller's rotation and for reducing torsional vibrations that might be imparted, a mechanical coupler is intervened. There are many setups for a mechanical coupler, the author selected a coupler component that resembles two splines meshed and between the meshing a flexible-rubber material component is placed.

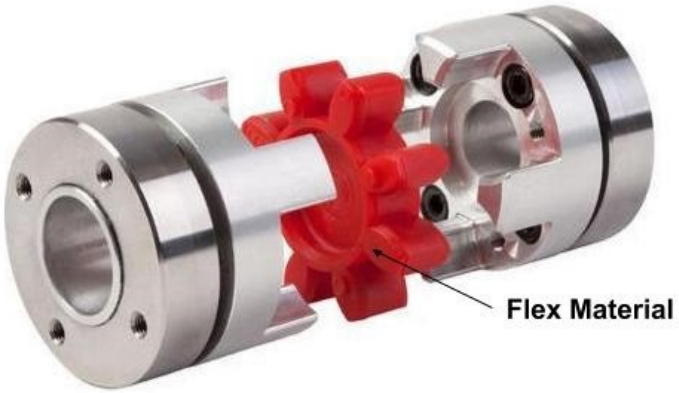

Figure 36: Jaw-type mechanical coupler. It is used for damping torsional vibrations between the connected shafts. [Source: https://www.smlease.com/entries/mechanism/what-is-mechanical-coupling-types-applications]

The hole in the eye of the blower serves the purpose of mounting the impeller to the shaft. To enhance the structural integrity of the blower assembly, especially given the substantial diameter of the impeller, a circular plate flange is attached to the back plate of the blower using bolts. This circular plate is responsible for securing the shaft. The shaft consists of two parts so the jaw-type mechanical coupler can be mounted. The assembly of the blower with the shaft, as described above, can be seen in the following *Figure 37* in exploded view.

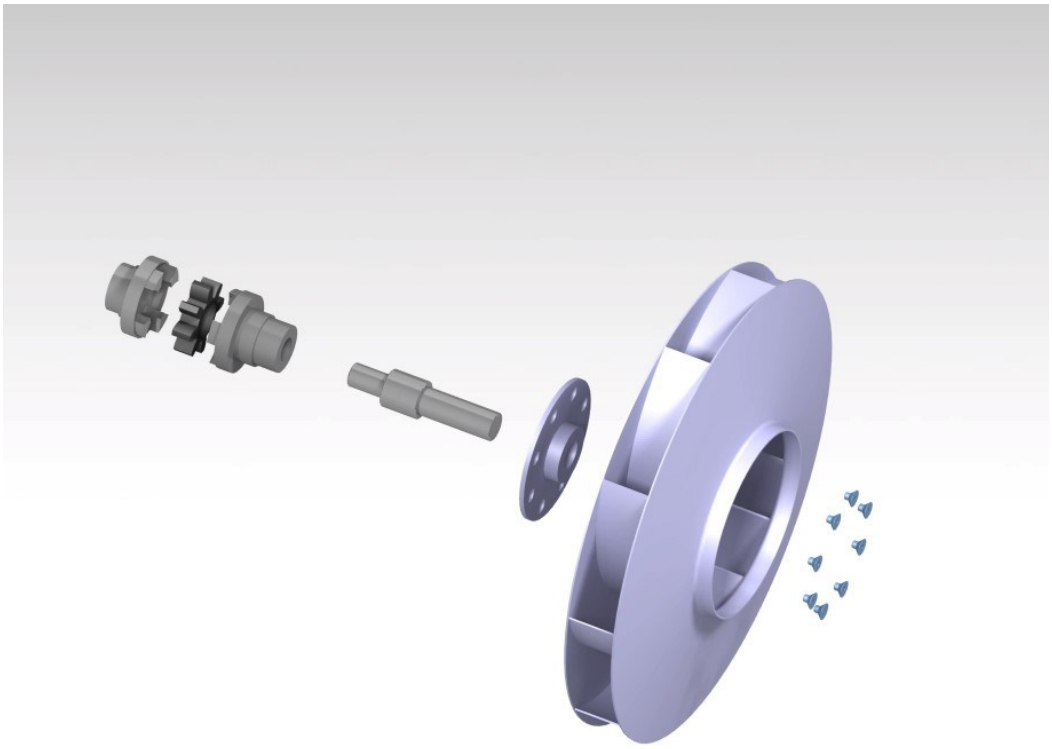

Figure 37: Exploded view of the assembly of the impeller with the shaft. At the end of the shaft a jaw-type mechanical coupler is connected.

The actual result of the impeller assembly with the shaft is shown in the following *Figure 38*.

Figure 38: The blower is mounted to the shaft. Also, the shaft is supported to the bottom flange of the casing.

3.7.3. Cyclone

The cyclone formation consists of two cone shaped sheet metal flanges and one cylindrical. Also, there is a cylindrical pipe for the fan's inlet and one cylindrical pipe for the mounting of the hose. All the above components were shaped by cutting a $2\ mm$ flat steel plate layout of the shape and shaping into the corresponding cone or cylinder by using the roll plate machine. The two cones were welded in the bottom and top side of the cylindrical barrel to form the basic formation of the cyclone, as seen in the following *Figure* 39.

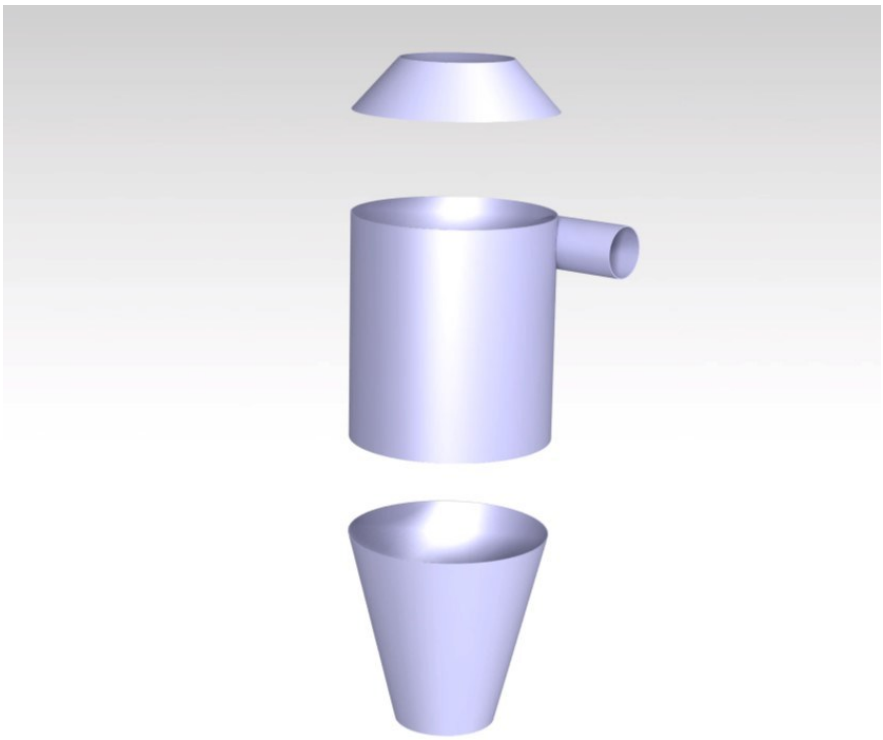

Figure 39: Metal sheets formed into two cones and one cylinder for the cyclone formation.

On the top of the cyclone, a rectangular steel plate is welded for the connection and support of the impeller's casing to the top of the cyclone. Also, another rectangular steel plate is welded at the bottom of the cyclone for the connection of a rotary valve.

Figure 40: Rotary valve component assembly. It consisted of a shaft with radial vanes and a casing. [Source: https://www.thomasnet.com/articles/pumps-valves-accessories/all-about]

Finally, inside the cyclone component a cylindrical pipe (vortex finder) is inserted for improving the flow conditions inside the cyclone, as described in section *3.5*.

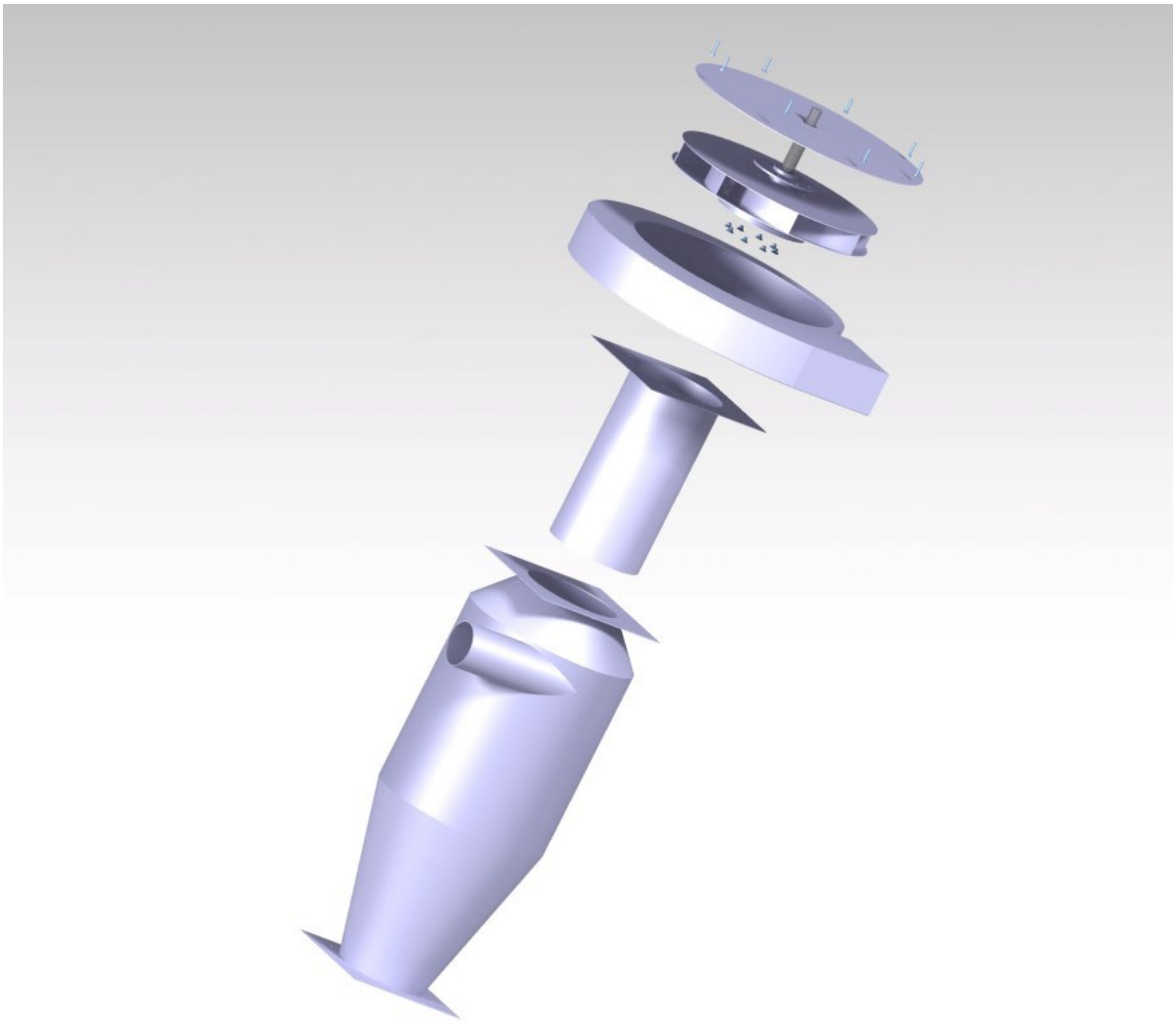

Figure 41: Assembly of the aspirator device with cyclone. The components displayed in this figure from bottom to top are the following: Cyclone, inlet pipe (vortex finder), casing, impeller's blower, axis (with coupler) and the casing top flange.

For a better understanding of the way that the above components fit together, how the geometries are formed insider the cyclone component, a mechanical drawing is given in *Figure* 42. This figure includes not only the front view of the cyclone aspirator device but also a section view, illustrating how the inlet pipe is attached to the cyclone using the rectangular plate as support. Moreover, the same rectangular plate of the cyclone acts as a support for mounting the impeller's casing. A detailed view is provided to showcase the location where the lip of the impeller fits through the casing opening.

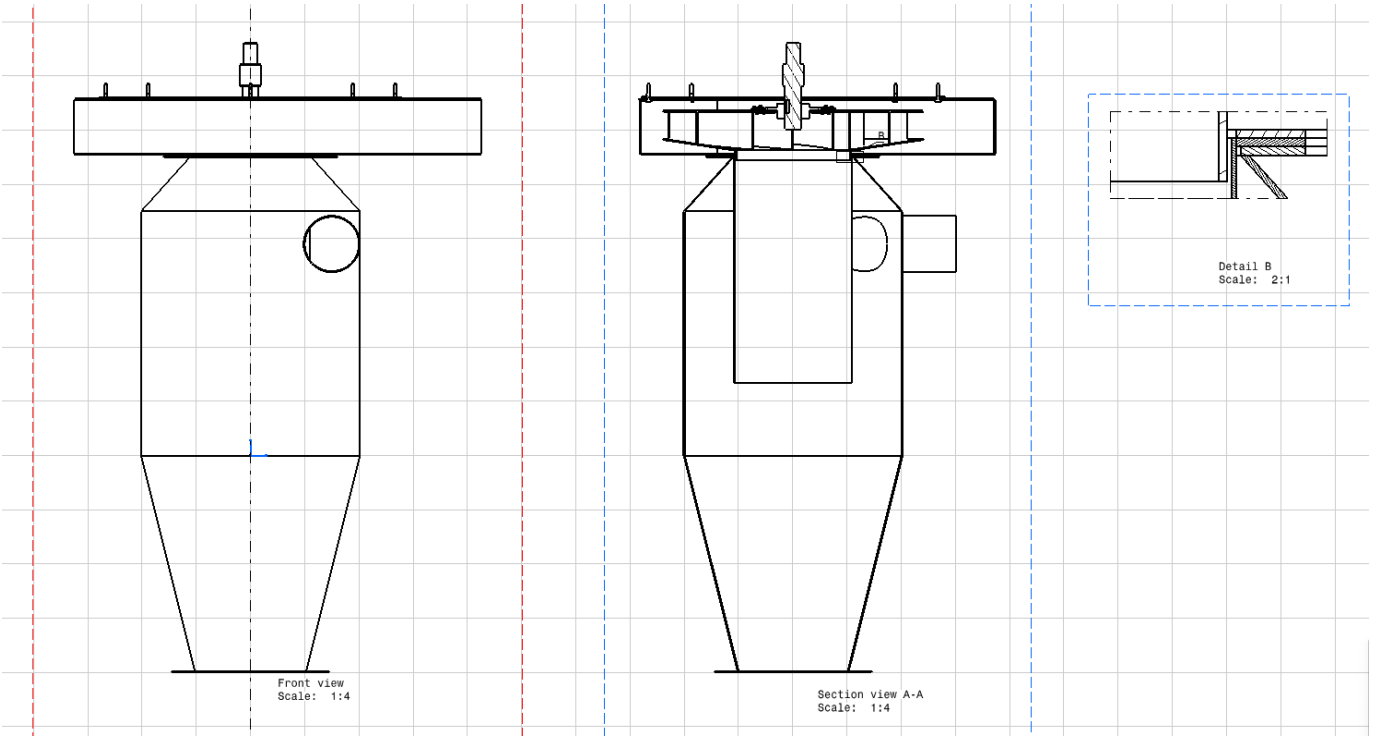

Figure 42: Mechanical drawing of the assembly of the cyclone aspirator device. The section view aids in illustrating the fitting of the inlet pipe inside the cyclone component. A detailed view in the area of the support of the casing to the cyclone is also included to help visualize how the fan's lip is threaded through the casing.

3.8. Aspirator device design without cyclone component

In the author's second endeavour to construct the aspirator device, the crucial change was the replacement of the cyclone component with a sizable rectangular box, similar to an inlet box of a duct system. The much bigger cross-sectional area of the rectangular box results in a very low air velocity, so the solid particles are no longer suspended in the air stream and drop in the bottom of the rectangular box container. The deleafing feature is not present in this setup as there is no mechanism for the separation of the olive leaves from the solid particles. This feature was abandoned by the author due to the complications it presented and the significant difficulty in modelling it.

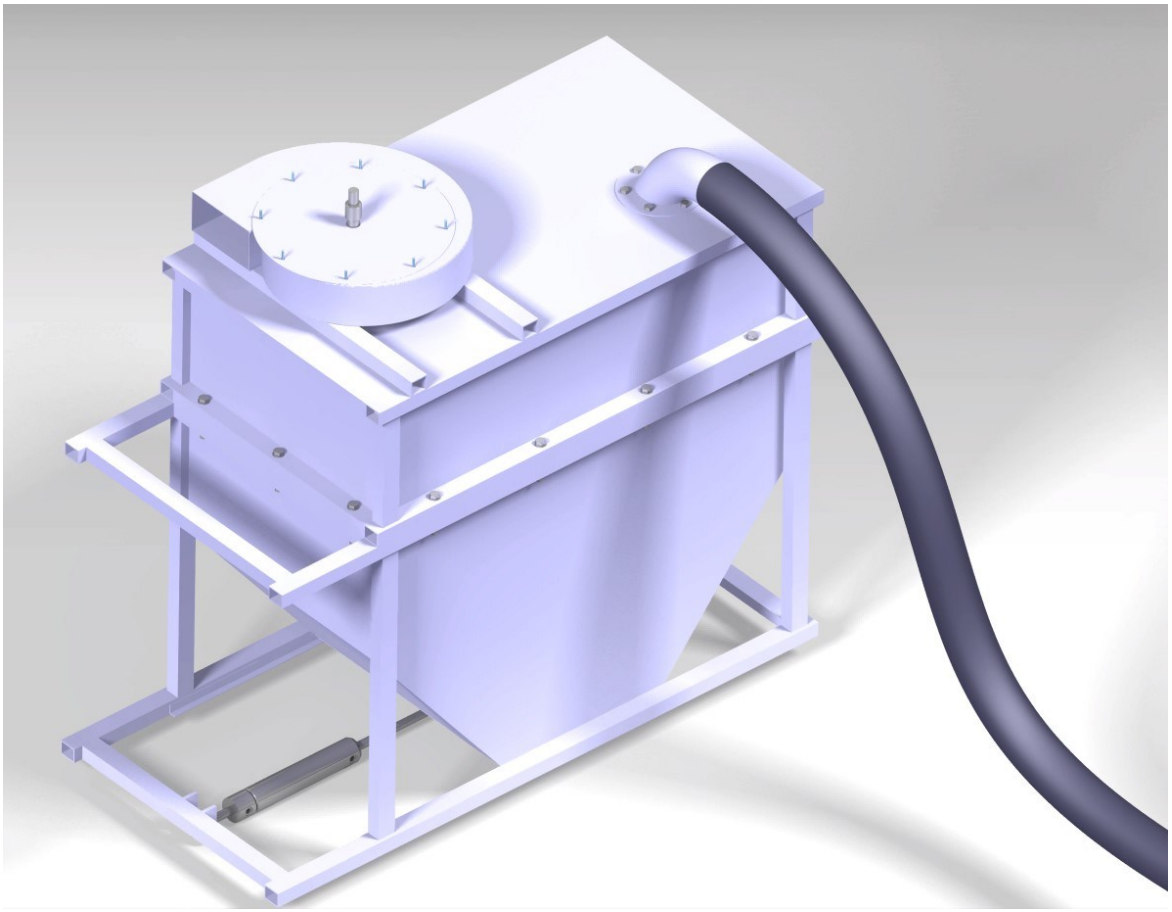

Figure 43: Aspirator device with rectangular collecting bin, designed in CAD software for prototyping.

This setup provides better terms for modelling and prediction of the operating conditions for the following reasons:

1. The geometrical domain of the rectangular box imposes more straightforward flow conditions compared to the cyclone. As seen in *Figure 25,* the cyclone's geometry creates multiple types of flow. Instead, when the air reaches the rectangular box, due to the large cross-sectional area, the air velocity is near zero, in most regions of the container.
2. The point at which the separation of solid particles from the airstream occurs can be assumed to be the junction where the hose meets the rectangular box.
3. Less operating parameters are required for the design of the rectangular box, compared to the cyclone. In addition, most of the dimensions of the rectangular box do not play such a crucial role for the air flow operation.

The geometrical design of the rectangular box bin features an inclined plane at its lower section to ease the unloading of the collected olive fruits. The floor, made of steel plate, is not permanently fixed to the bin, allowing it to be moved. Additionally, a hydraulic cylinder is installed, which can be activated to initiate the unloading process. Lastly, the rectangular bin is constructed as two separate components: an upper part and a lower part that are securely fastened together. This design choice is intentional, as it results in a more robust solution, facilitating simpler assembly and component fitting, enhancing structural integrity, and enabling easier disassembly in the event of a malfunction.

A prototype design of the assembly of the collecting bin, the moving floor, the hydraulic cylinder and the impeller assembly can be seen in *Figure* 43. In addition, *Figure* 44 shows the moving floor plane.

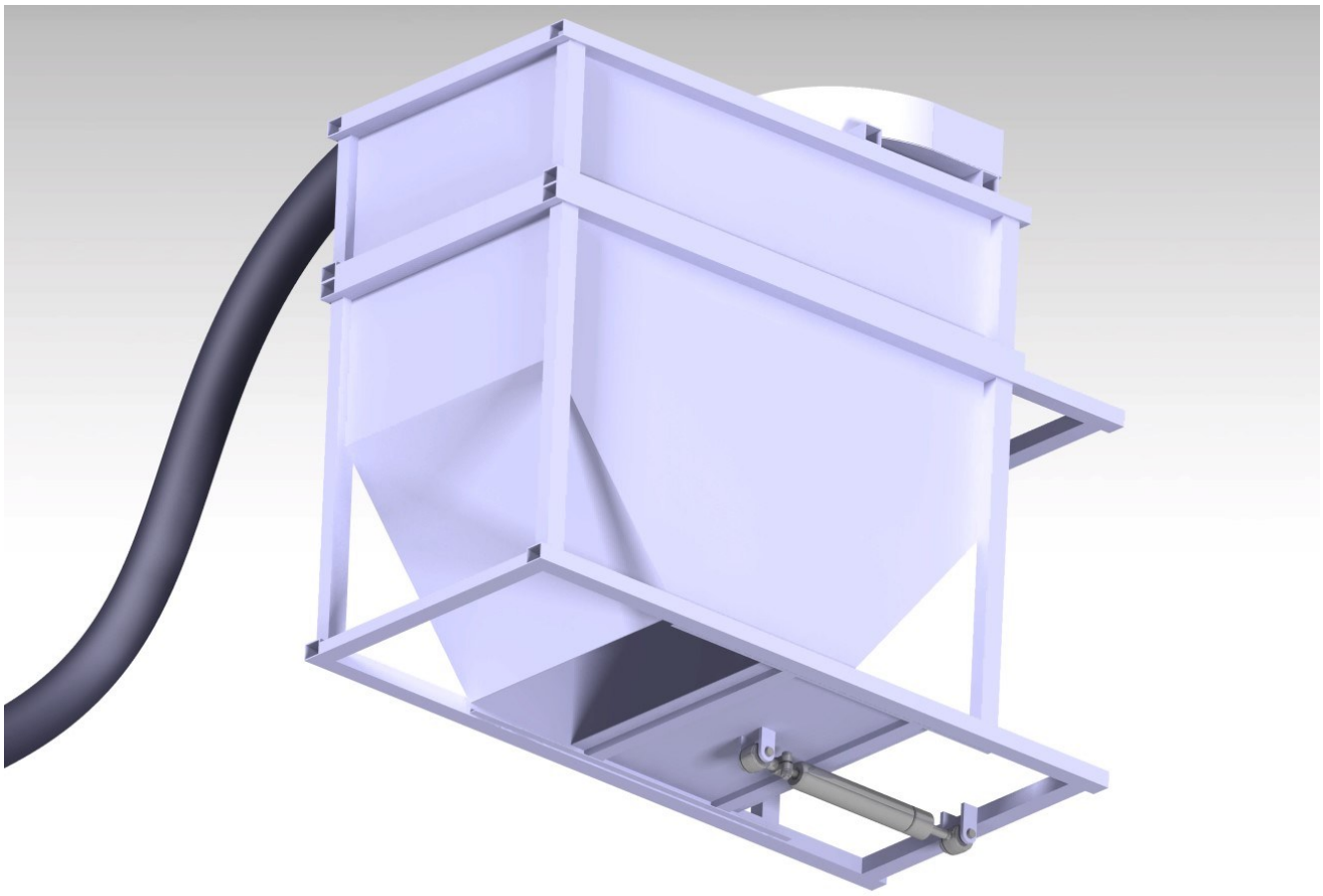

Figure 44: Bottom view of the aspirator device. The floor plane can be moved by the hydraulic cylinder for the unloading process.

The space within the collecting bin's frame, as depicted in the left part of the figure above, serves as the installation area for the oil tank. This tank contains hydraulic fluid necessary for two key functions: one is for the operation of the hydraulic cylinder that controls the opening of the collecting bin floor gate, and the other is for the operation of the hydraulic motor that powers the impeller.

Inside the collecting bin, two additional components are housed: the impeller's flange and the inlet hose's flange diffuser. These diffusers serve two purposes that enhance the efficiency of the air flow. First, in the case of the impeller's diffuser, it aids in directing the air flow uniformly into the impeller. This is particularly beneficial as the air flow needs to change direction to enter the impeller, and the diffuser ensures a more even distribution of airflow, rather than a concentrated flow at the centreline of the inlet. This behaviour can be clearly illustrated in the following *Figure 45*.

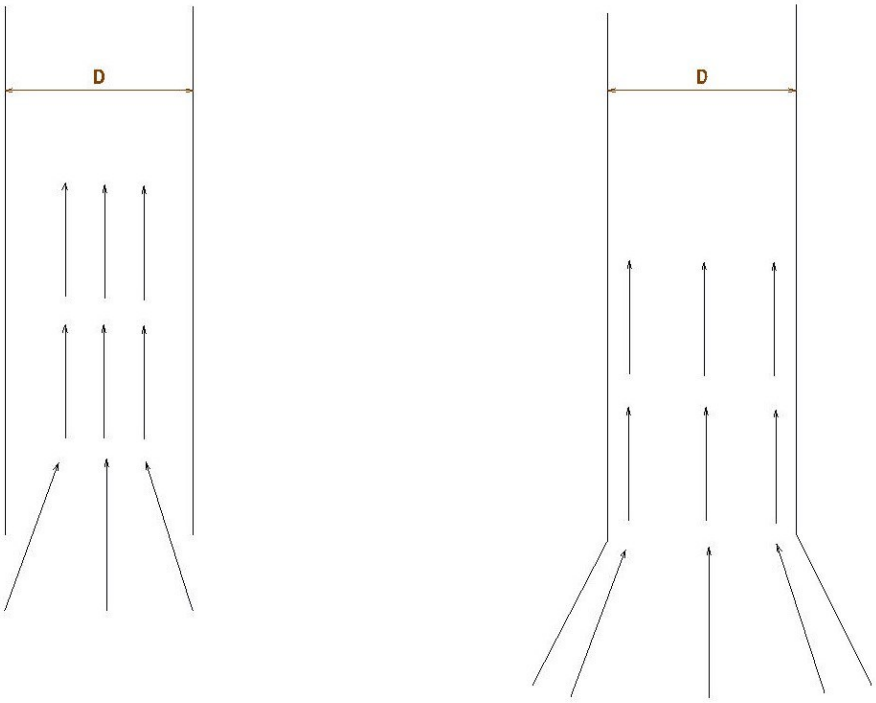

Figure 45: Demonstration of the flow field in the absence of the diffuser (left) and with a diffuser (right). The diffuser enables a smoother transition of the flow.

The second feature that both diffusers offer is the ability to achieve a smooth acceleration of the air flow in the case of the impeller's diffuser and a smooth deceleration of the air flow in the case of the inlet hose's flange diffuser. When acceleration or deceleration of the air flow isn't adequately smoothed out, turbulence and secondary flows increase their intensity, resulting in higher energy losses and unwanted flow patterns. In the following figures, the geometrical formation of the impeller’s diffuser and the inlet hos flange’s diffuser can be seen.

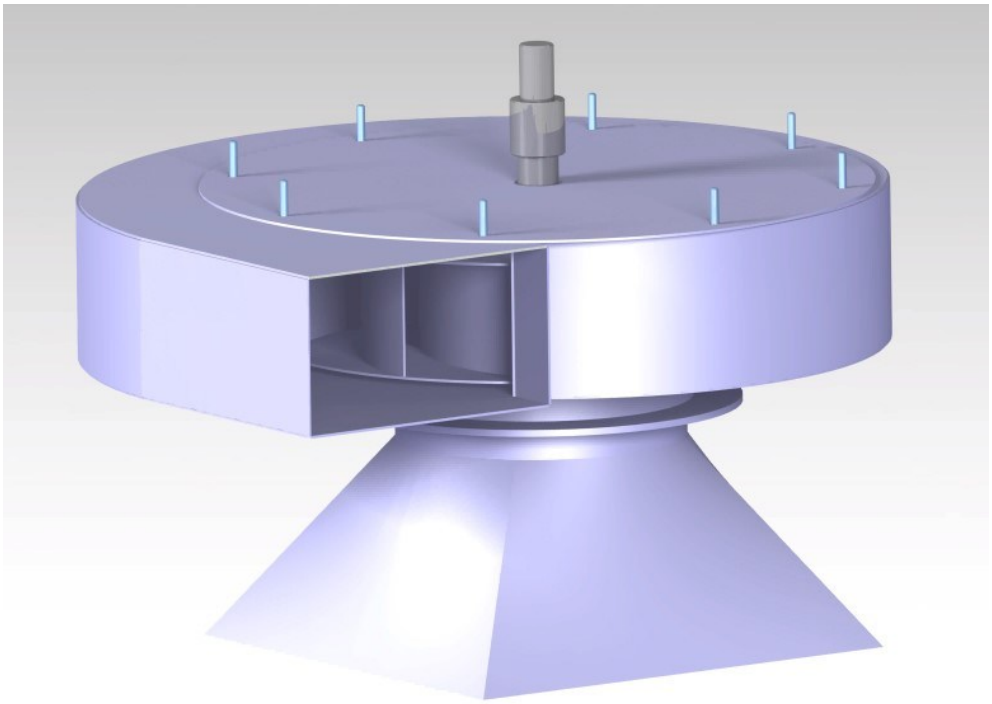

Figure 46: Impeller assembly. The blower lies inside the casing and the impeller's inlet is connected to the diffuser.

The inlet flange of the hose features a design that gradually increases the cross-sectional area towards the end, functioning as a diffuser to gently decelerate the flow. Furthermore, the hose's inlet flange has another purpose that is to connect the hose with the collecting bin. This connection inevitably introduces a bend in the piping system. The formation of the bend was chosen to be a 45^0 degree turn rather than a 90^0 degree turn, as seen in *Figure* 47. This choice was made in order to reduce the collision of the solid olive fruit particles and the minor losses of the airflow due to friction and the inertial forces that make the flow non-uniform during a turn.

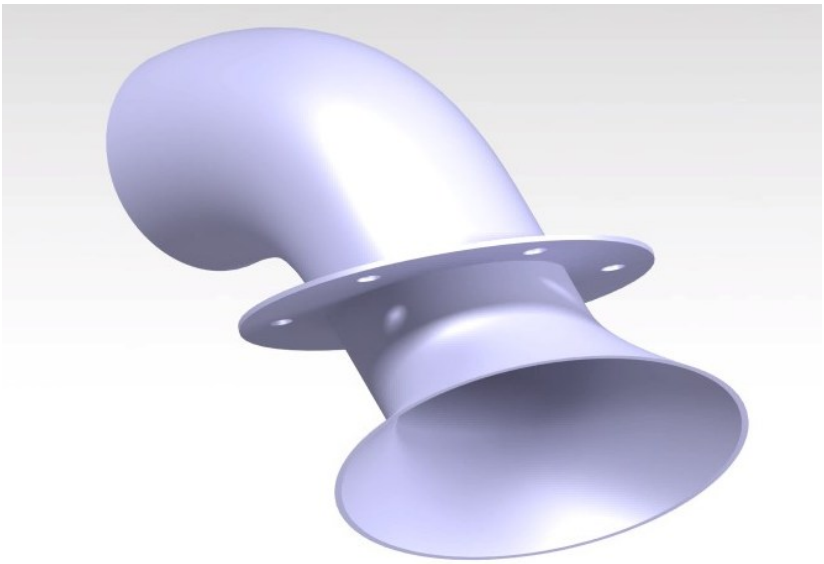

Figure 47: Hose's inlet flange with a diffuser

The impeller's design has followed the same design as the one used in the aspirator device with a cyclone, so the design can be seen in *Figure* 15. Although, some modifications were made in order to increase the air flow that the impeller induces and also its efficiency. The inlet and outer diameters and the leading and trailing angles remained the same as the previous design. The change in the parameters is about the width of the fan's blade in the inlet b_1 and the outel b_2.

Initially, the inlet at the outlet width was decided to be equal, meaning:

$$b_1 = b_2 \tag{3.13}$$

According to bibliographic research for fan design [9], the above condition offers some benefits compared to the $b_1 > b_2$ condition, besides the easier manufacturing process. The $b_1 > b_2$ condition is used frequently, as it keeps constant the cross-sectional area of the channel between two consecutive blades, in which the air flows. The fact that the cross-sectional area remains constant results in better efficiencies due to the fact that no deceleration occurs, thus no pressure gradient is created opposing the airflow and generating reversed flow currents. In practice, the above reasoning overlooks the fact that after the airflow reaches the blade's tip, a sudden expansion occurs as it is no longer bounded by the blower's shroud and blades. At that point, only the blower's casing confines the flow, which has much larger width. Therefore, the condition of (3.13) can result in practice in higher efficiencies, as the deceleration of the flow is smoother and the sudden expansion at the blade tip is less severe.

The blade angles at the leading and trailing edges also affect the deceleration of the flow inside the channel created by two consecutive blades. In order to ensure that the deceleration of the flow is occurring gradually and at an even rate, as is desired according to the paragraph above, a simple procedure can be employed. At several points along the blade channel, circles are inscribed, meaning that they are bitangential to the two consecutive blades. These inscribed circles can be seen in *Figure 48*.

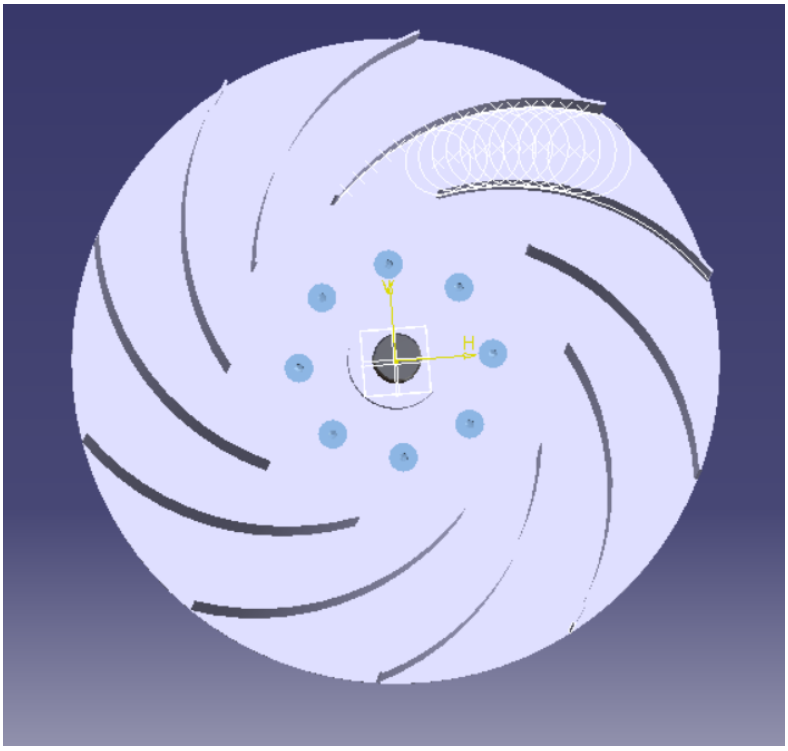

Figure 48: Centrifugal fan with back curved blades. Inside the blade channel, inscribed circles are drawn.

After drawing the inscribed circles, the next step is to calculate the area of the flow at each point, by multiplying the diameter of each circle with the blade width that corresponding to the circle's center. After that, for each area, a diameter of a circle with equal area is calculated (equivalent diameter). Then the equivalent diameters are plotted against the centerline of the channel, therefore a cone is obtained. Each point should correspond to a cone angle less than 7^0, if not, the design should be revised.

For the implementation of the above method, the value of the blade width is needed, therefore before the numerical calculations of the above method, the blade width $b_1 = b_2 = b$, will be determined. As mentioned previously, the impeller of the second aspirator device, which features a rectangular collecting bin instead of the cyclone, will maintain identical design parameters for the impeller, with the exception of the blade width that will be increased. The choice for a larger value of the blade width was made in order to increase the airflow. Again, according to the bibliography [9], there is an upper limit to the blade width, given in the following relationship.

$$b \leq 0.46\, D_1 \tag{3.14}$$

The formula above is an empirical relationship derived from experimentation. However, it highlights an important aspect of the airflow behaviour as it enters the impeller. Upon entering the impeller's shroud, it makes a 90^0 turn to follow the blade channel. Due to the airstream inertia, the airstream is not evenly distributed across the blade width but rather is concentrated in the impellers back plate, leading to undesired flow conditions. Therefore, exceeding the blade width limit, specified by the formula above, could potentially reduce the hydraulic efficiency of the impeller, leading to an increase in included flow only in theory.

The author decided to set the blade width equal to 40% of the inlet diameter D_1, hence $b = 0.4D_1$. Now the procedure of the inscribed circles can take place, in order to validate that the blade channels offer a gradual deceleration of the air flow.

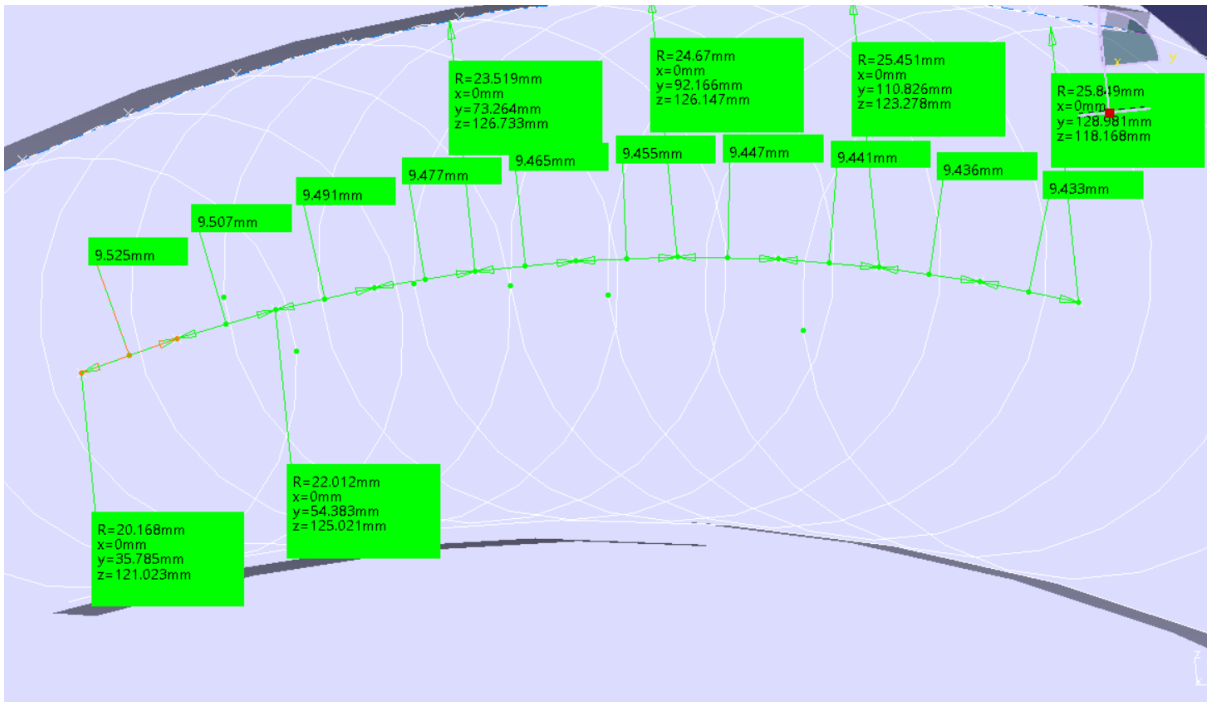

Figure 49: Measurements of the inscribed circles radii and distances between circle centers.

The above measurements were placed in the following table, where the calculations of the equivalent diameter took place.

Table 8: Inscribed circles procedure

Inscribed circle Radii (mm)	Center distance (mm)	Area of inscribed circles (mm^2)	Cones inclination in degrees
20.168	-	1694.11	-
21.131	9.525	5576.34	5.77
22.012	9.507	5808.83	5.29
22.809	9.491	6019.15	4.80
23.519	9.477	6206.52	4.28
24.14	9.465	6370.40	3.75
24.67	9.455	6510.26	3.21
25.108	9.447	6625.85	2.65
25.451	9.441	6716.36	2.08
25.698	9.436	6781.54	1.50
25.849	9.433	6821.39	0.92

The procedure validates the blade channel design in terms of decelerating gradually the airflow, so there is no need for changing the leading and trailing edge angles for making a narrower blade channel. Therefore, the design parameters of the centrifugal fan for this aspirator device are given in the following table.

Table 9: Design parameters of the centrifugal fan of the aspirator device with the rectangular collecting bin. The only variations from the cyclone's aspirator device parameters are underlined, which correspond to the blade width.

Parameter's description	Parameter's value
Inlet diameter $\mathbf{D_1}$	$210\ mm$
Inlet blade width b_1	$\underline{80\ mm}$
Outlet diameter D_2	$490\ mm$
Outlet blade width b_2	$\underline{80\ mm}$
Blade's leading-edge angle β_1	30^0
Blade's trailing-edge angle β_2	25^0
Rotational speed n	$2800\ rpm$

3.9. Operation of the aspirator device with rectangular box bin

The design of the rectangular box aspirator was anticipated to have a higher free air velocity compared to the cyclone aspirator device. This expectation stemmed from the fact that the impeller in the second aspirator device featured a larger blade width. Additionally, the system's pressure drop was expected to be lower because the box's geometry offered less resistance to the flow. These factors were all projected to contribute to a greater mass flow ratio, which was the desired outcome. The following figure (*Figure* 520) shows the complete setup of the aspirator device with a rectangular bin and the hydraulic system for powering the impeller and hydraulic floor gate.

.

Figure 50: Aspirator device with rectangular box. The hydraulic system for the impeller's rotation is also visible.

Following the impeller's operation, the free air velocity was measured, and it exceeded the required level, reaching a significantly higher value, $v = 60\ m/s$. This excessive velocity led to a substantial pressure drop due to friction losses, which are proportionate to the square of the airstream velocity. Moreover, the transportation of olive fruits did not exhibit the expected improvement despite the increased velocity. Upon further observation, it became evident that while the olive fruits were initially introduced into the hose at a satisfactory rate, they tended to form immovable beds within the hose, particularly in sections with excessive curvature.

The hose's path is not ideal for modelling as not entire horizontal, vertical, or even inclined. The curves within the hose can result in significant flow separation, leading to non-uniform airflow. Additionally, these curves provide ample opportunity for extensive and frequent collisions between the olive fruits and the hose walls. As a result, the olive fruits lose kinetic energy and become trapped in the curved sections, obstructing the airflow and causing the fruits to once again become suspended in the air stream.

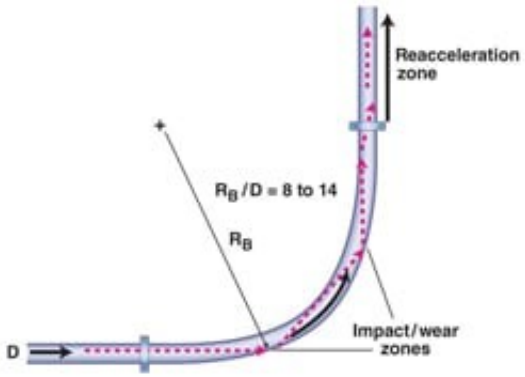

Figure 51: The piping system bends introduce several collisions between the solid particles and the walls of the pipes.

To mitigate the issues previously mentioned, a solution was implemented: increasing the hose diameter and shortening its length. These modifications offer several advantages. Firstly, the larger diameter reduces the air velocity, resulting in lower friction losses, which are proportional to the square of the air velocity. It also provides more space for the olive fruits to travel before impacting the hose walls, reducing the number of collisions. Secondly, the shorter hose length creates a more favourable hose path by reducing the number of curves that form in a longer hose. It's important to note that the pressure drop, caused by friction and solid particle impacts, is also proportional to the hose length. The following figure (*Figure* 52) shows the aspirator device in action, operating in the field, after the hose's modifications. It's evident that the hose features fewer curves, and the reduced length doesn't hinder the device's access to the olive fruit pile.

Figure 52: Aspirator device operating on the field. The hose length was shortened to minimize curve formation in the hose's path.

After those modifications, the free air velocity was reduced as expected and the efficiency of the aspirator device was improved, as the solid mass flow rate increased. The data from the operation of the aspirator device is presented in the following table.

Table 10: Aspirator device with rectangular box operational data.

Hose diameter D_{hose}	Impeller rotational speed n	Free air velocity v	$\dot{m}_{solid}$
$\mathbf{130\ mm}$	$2800\ rpm$	$55\ m/s$	$100\ kg/min$

As demonstrated in the preceding table, the solid mass flow rate has experienced a significant increase. The current solid mass flow rate is highly satisfactory, enabling efficient field operations and significantly reducing the labor time and effort required for olive fruit collection. A validation of the operational data is the calculation of the mass flow ratio μ.

$$\mu = \frac{\dot{m}_s}{\dot{m}_f} = \frac{\frac{100}{60}\,kg/s}{(1.184\ kg/m^3)\left[\pi\left(\frac{0{,}13}{2}m\right)^2\right]55\ m/s} = 1.93$$

The mass flow ratio is close to the value of $2:1$, indicating a solid-to-air mass flow rate, which is a preferred ratio for dilute-phase conveying of large particles, as suggested by the bibliography.

3.10. Manufacturing process of box aspirator device components

The manufacturing process of the impeller's casing is identical to the casing of the cyclone aspirator device. This also applies to the impeller's blower, with the only exception of the flat shroud. The impeller's blower of the box aspirator device has an equal width of blades at the inlet and the outlet of the fan, so there is no need for a conical-shaped shroud, resulting in a simpler manufacturing process. Moreover, the connection of the impeller's blower to the hydraulic motor was executed in the same manner as in the cyclone aspirator device, involving the use of a circular plate flange and a mechanical coupler. The assembly of the box aspirator device is given in the following figure.

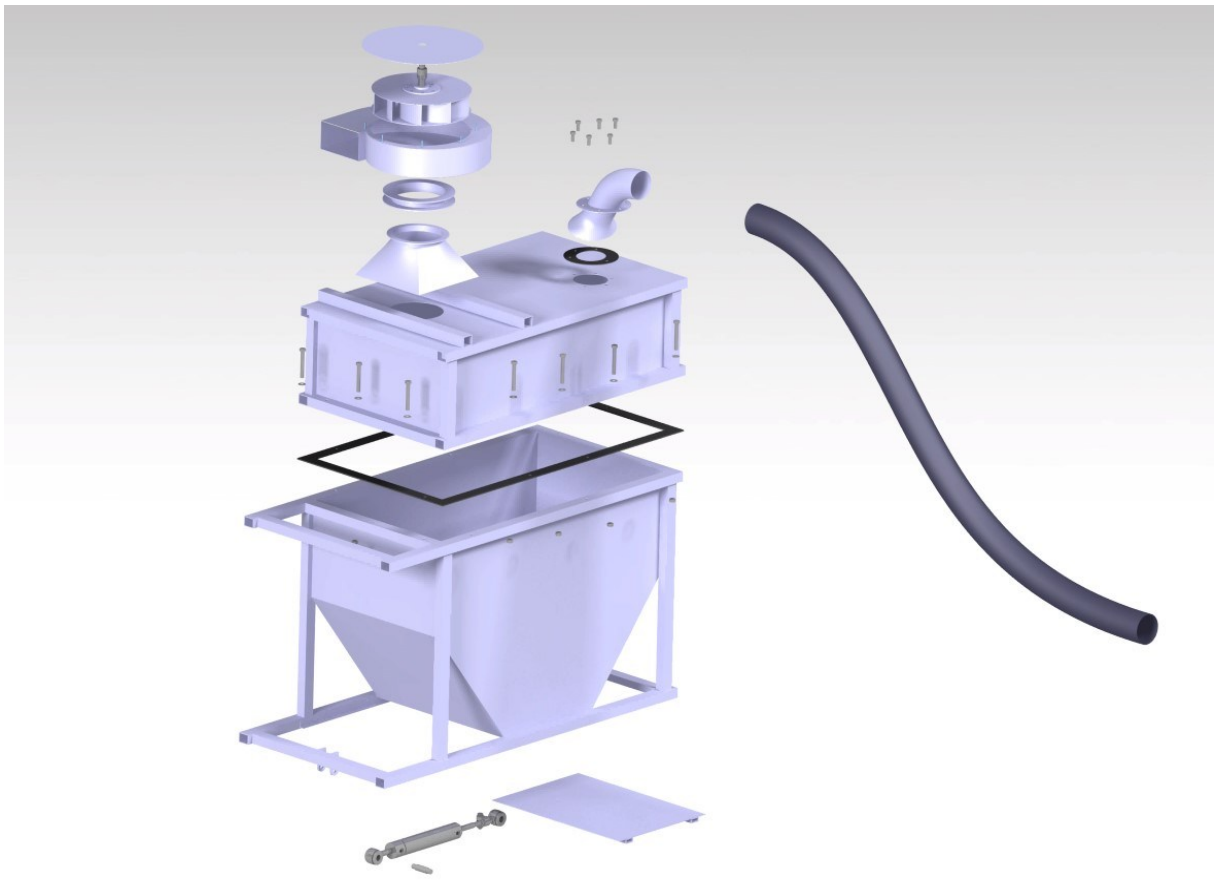

Figure 53: Exploded view of the box aspirator device.

3.10.1. Impeller's diffuser

The mounting of the impeller's casing in this setup is done with the assistance of a small length cylindrical ring, as opposed to the case of the cyclone aspirator device, where an inlet pipe was employed. This variation is necessitated by the mandatory use of a diffuser in the inlet of the impeller due to the air flow conditions within the box, as detailed in section *3.8*. For the same reason, a diffuser was inserted at the hose mounting to the box. Due to the impeller's diffuser being a square-to-round duct, the manufacturing process required the design of the sheet metal layout first. The method for unfolding the square-to-round duct uses the process of the triangulation of the surface of the duct, as seen in the figure below, where the top view of the surface of the duct is mapped to the layout design.

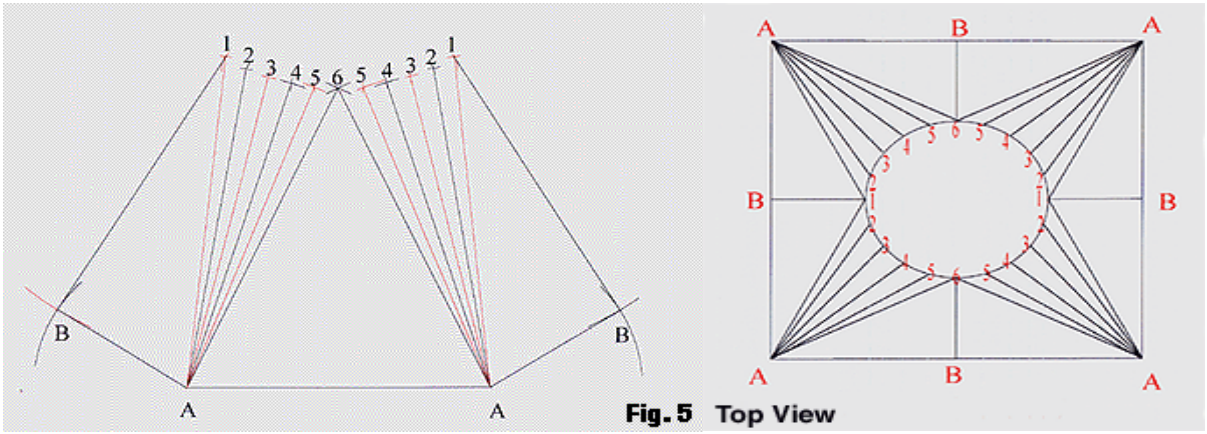

Figure 54: Using triangulation, the top with of the square-to-round duct numbered points are mapped to a flat layout. [Source: www.sheetmetalworld.com/sheet-metal-news/fabrication-tutorials/22-sheet-metal-tutorials/5962-how-to-develop-a-square-to-round]

To streamline the parametrization process, the author employed a shortcut by utilizing a command in the CAD software. This approach proved efficient, especially considering the prior effort invested in prototyping and parametrizing the square-to-round duct with the CAD software. The command $unfold$ can produce the flat layout of a $3D$ connex and manifold surface. So, by extracting the surface formed by the square-to-round duct and unfolding that surface the following layout was produced, as seen in *Figure* 55.

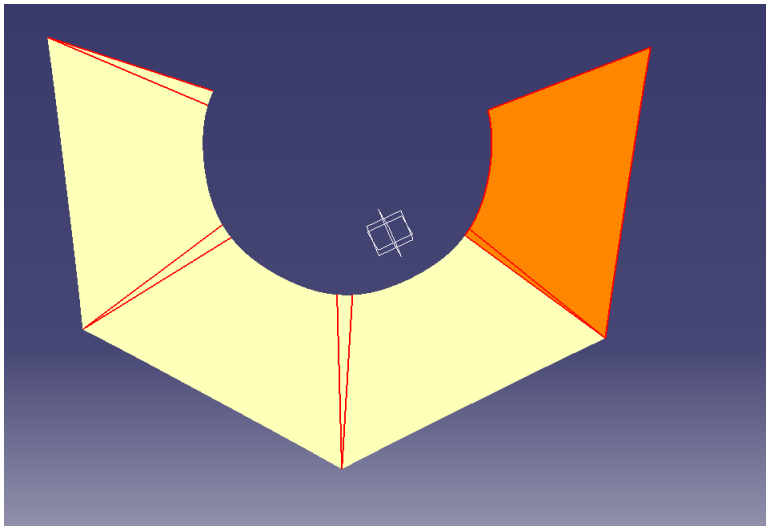

Figure 55: Layout of the square-to-round duct produced in CAD software with the unfold command.

The layout was exported in $.dxf$ format and fed to a CNC plasma cutter. With the help of the guidelines shown in *Figure 55*, the bends were made, giving the final desired shape. The last thing was to weld the two ends together.

3.10.2. Hose diffuser

The manufacturing process of the hose diffuser involved two steps, as the diffuser comprises two formations: the pipe bend and the cross-section increasing part that functions as a diffuser. Firstly, for the bend part formation, the radius of the bend curvature was measured using the CAD prototype design, as shown in the following figure. Subsequently, a straight pipe section with length equal to $s = R * \theta$ was rolled into the pipe bending machine.

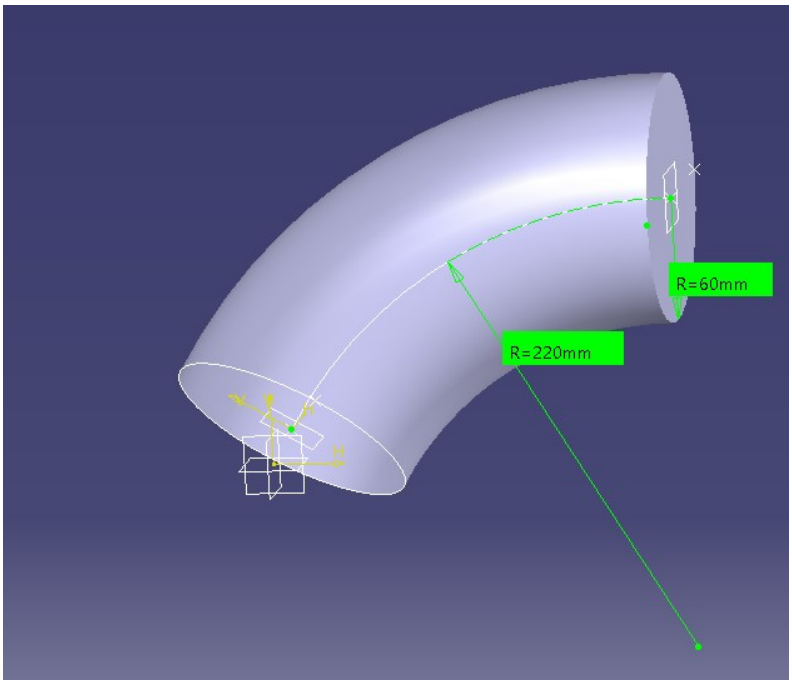

Figure 56: Measuring the curvature of the pipe bend using CAD software.

Due to the bend radius being more than two times the pipe radius, the utilization of the pipe bending machine was appropriate. The second step involved forming the diffuser part, which commenced with creating a cone from a metal sheet. Subsequently, using a hydraulic press, the cone-shaped pipe was gradually flattened in one direction, resulting in an ellipse-like profile. Finally, the two parts were welded together.

3.10.3. Collecting Box

In this aspirator device setup, the rectangular box bin is the substitute for the cyclone component and one of the advantages, as mentioned in section *3.8*, is the simpler manufacturing process. To facilitate assembly and maintenance, the component was fabricated as two parts joined together with bolts: an upper part and a lower part. The manufacturing of the lower part started with the construction of the frame made from steel beams welded together. Afterwards the bin was formed by steel plates welded along the beam frame. The frame is extended from the one side of the bin for supporting the hydraulic cylinder that is responsible for opening the floor gate. Also, the space formed can serve for the support of the hydraulic system's tank. The assembly of the lower part of the rectangular box bin is shown in the following *Figure* 57.

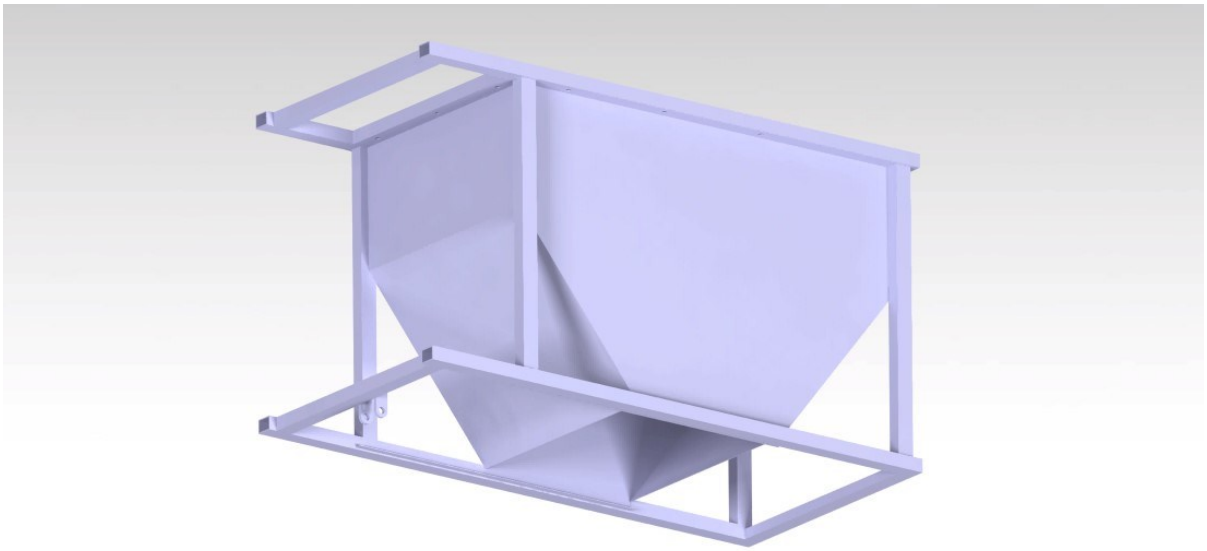

Figure 57: Lower part of the collecting bin box. The frame made of steel beams also supports the hydraulic cylinder for opening the floor gate, and the floor gate.

The upper part of the collecting bin box was constructed by first welding the steel beams for making the frame and then the steel plates for forming the upper part of the bin. In addition, the top of the upper part is where the casing will be supported and the Hose diffuser, hence opening where made for the fitting of the casing and the hose diffuser.

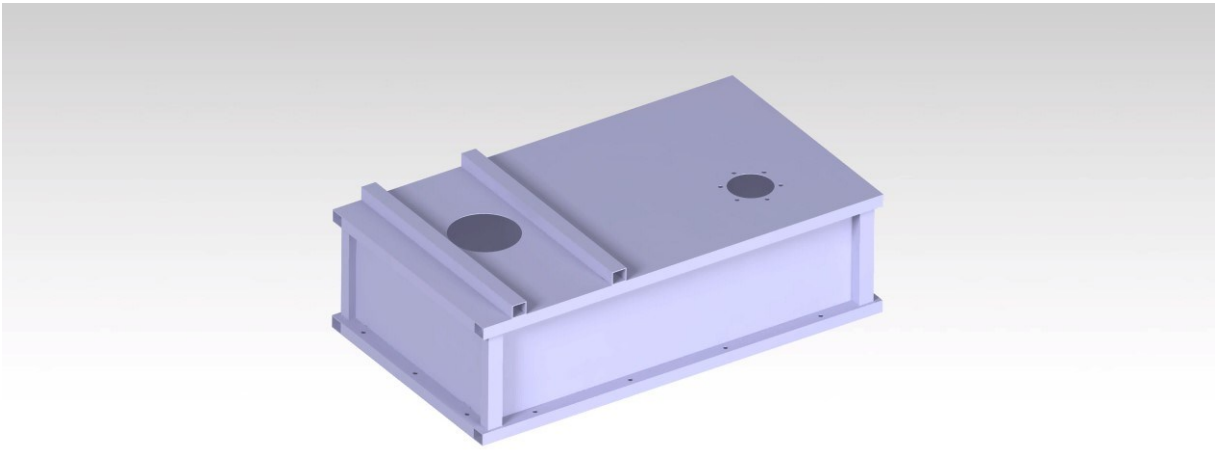

Figure 58: Upper part of the collecting bin box. The left opening is for the impeller's casing fitting and the right opening for the hose diffuser mounting.

Figure 59: Box aspirator device completed assembly.

3.11. Comparison between the two aspirator devices setup

After a thorough description of the operational conditions and a comprehensive examination of the performance of both aspirator device configurations, it becomes evident that the aspirator device without the cyclone component outperforms its counterpart in various aspects.

In higher detail, it is noteworthy that the rectangular box aspirator device achieves a solid mass flow rate approximately **five times higher** than that of the cyclone aspirator device, despite both devices employing nearly equal free air stream velocities and identical impeller rotational speeds. The solid mass flow rate stands out as the paramount performance metric, as it exerts the most substantial influence on the productivity efficiency of the aspirator device. Productivity efficiency, in turn, serves as the pivotal criterion that potential customers rely on to determine whether the investment in the aspirator device is worthwhile, as it directly impacts the device's ability to carry out the task of olive fruit collection in a time-saving manner.

The reasons behind the superior performance of the rectangular box aspirator device in comparison to the cyclone aspirator device are manifold, and some of these have been previously discussed in the text. The most significant factor, as extensively analysed in section 3.5, is the complex geometry of the cyclone, which results in a higher pressure drop within the system. Furthermore, the cyclone component introduces various undesirable flow patterns that do not contribute to the conveying process.

An additional, previously unmentioned factor, stemming from practical considerations, relates to the unloading process of the olive fruits from the aspirator device, which is facilitated by the rotary valve component. The cyclone component has no significant capacity storage, so the unloading of the collected olive fruits takes place almost in a continuous manner. This unloading process happens thanks to the rotary valve component which is mounted at the bottom of the cyclone bin, as shown in *Figure 60****Error! Reference source not found.***. The rotating vanes inside the rotary valve casing, extract the olive fruits in a constant rate without interrupting the aspirator device operation. In addition, they provide sealing from the outside environment preventing unwanted airflow entering from the bottom of the cyclone bin due to the lower pressure inside the cyclone component.

Figure 60: Rotary valve component, mounted at the bottom of the cyclone. The continuously rotating vanes inside the rotary valve casing unload the olive fruits at a constant rate. [Source for image: "crfcostruzioni.it"]

On the other hand, the rectangular box aspirator device has enough storage capacity, so that the unloading process can take place once the bin is filled, giving an interruption in the operation of the aspirator device. The unloading process happens thank to the floor gate at the bottom of the rectangular box, as has been demonstrated in *Figure* 44. Despite the presence of a brief interruption in its operation for the unloading process, the dead time of the rectangular box aspirator is a negligible fraction of the total operating time.

After clarifying the principles of the unloading process, it can be shown that even the rotary valve's unloading process has a small advantage in terms of time-efficiency, it creates a major problem in the operating conditions, as it can tamper the flow conditions inside the system, as it cannot provide the sealing standards that the floor gate does.

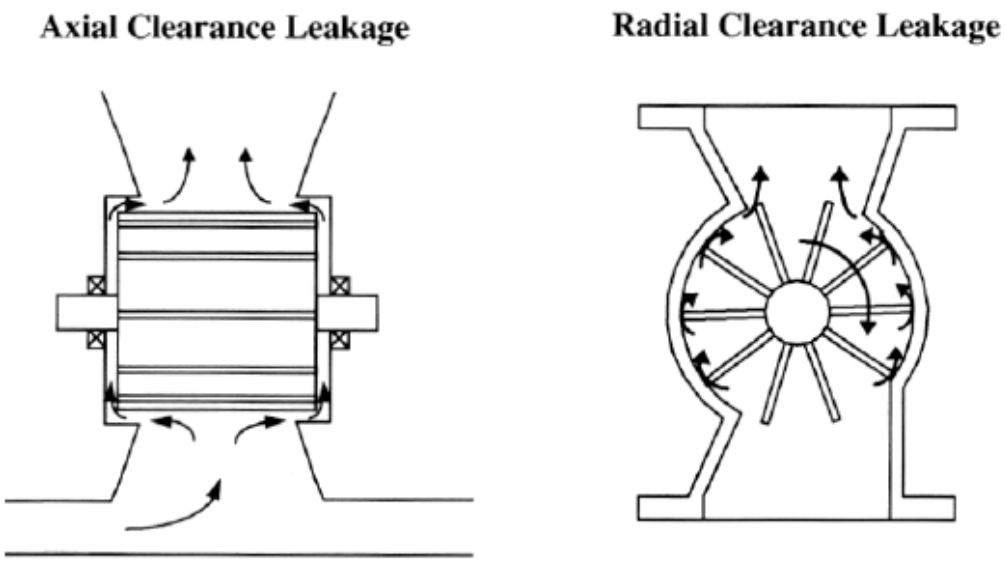

Figure 61: Rotary valve. The figure shows the rotating vanes inside the component. Due to their rotation, the vanes have some axial and radial clearance from the casing. [Source: "A NOVEL APPROACH TO ROTARY VALVE VENTING"]

As shown in *Figure 61*, due to the rotating operation of the rotary valve, the rotating vanes must have some axial and radial clearance from the casing. That means that the manufacture of the rotary valve component requires high precision tools for a decent result in sealing performance. However, even if a precise execution of the tolerance dimension is achieved, the nature of the operation of the rotary valve component cannot eliminate the clearance leakage.

Conversely, in the case of the rectangular box, clearance leakage can be entirely eliminated, as the floor gate movement is a simple low-speed slide, so the clearance that is needed for the movement can be effectively sealed with a suitable material, such as a solid rubber gasket, shown in the following *Figure 62*.

Figure 62: Solid rubber tape, for a sealing gasket. [Source: www.gteek.com/Rectangular-rubber-profiles]

To conclude, the prevention of the leakage flow gives another advantage to the rectangular box bin, over the cyclone bin, as the counter flow of the leakage reduces the hydraulic efficiency of the system, generating energy losses and destabilizes the flow conditions inside the bin, giving rise to undesired

flow patterns where solid particles can remain suspended instead of settling at the bottom of the collection bin.

The final reason that favours the rectangular box over the cyclone bin pertains to the design parameters. The cyclone component has a significantly larger number of parameters (as shown in *Table 6*), and their influence on the operation and flow conditions is more sensitive and unpredictable. Consequently, fine-tuning the parameters of the cyclone component to enhance performance is a more challenging task compared to the rectangular box.

Chapter 4. Conclusions

The two main configurations of an aspirator device were designed and manufactured for the purpose of this project: to investigate the working principles of the aspirator device. The process of parameter selection predominantly involved the examination of images of commercially available aspirator devices and experimentation with the dimensions of the components. This method yielded two aspirator devices capable of conveying olive fruits from the ground to the collecting bin, signifying a measure of success. However, it is evident that the optimal solution has not been reached, since the extensive utilization of the theoretical formulas in numerical calculations was limited. The formulas' role in this project was primarily confined to understanding how alterations in parameter quantities might influence the aspirator device's performance.

Through the operation of the aspirator device, it became obvious that a significant contributor to the pressure drop, caused by the transportation of solid olive fruits, is the multitude of collisions occurring between the solids and the inner wall of the hose. As seen in equation *(2.7)*, the pressure drop modelling due to the solid particles' interaction is relying on the solid friction factor λ_Z. This factor can only be determined experimentally by measuring a set of solid particle velocities c and the corresponding pressure drop. Those measurements require a sophisticated instrumentation and setup; however, they hold the potential for advancements in modelling the aspirator device and will pave the way for further optimization.

The theoretical framework of pneumatic conveying was applied to model the aspirator device, which shares some similarities with the pneumatic conveying system. However, two points of the aspirator device somehow deviate from the pneumatic conveying modelling. Initially, the hose curves were modelled by considering a specific hose shape. In reality the hose shape changes stochastically and besides from the fact that the curvature radius and curve length values are not always equal to the ones that were used in the modelling process, the fact that the hose's shape changes during run-time, disrupts the steady state of the airstream, introducing transition states that might lead to extra terms of pressure loss. The second point of deviation in the modelling is the solid mass load ratio. Although, this ratio is not predetermined in pneumatic conveying, there is a distinguishing feature of the solid feeder that can control the presence and feed ratio of solids in the piping.

4.1. Improvements

The following points highlight the most crucial steps that fulfil the objectives of this project:

1. The theoretical framework for the aspirator device, including formulas that can be applied during the initial stage of iterative design, even in the absence of prior experimental data.
2. The mechanical components required for the effective design and operation of the aspiration device, along with their manufacturing process, offering comprehensive documentation on the construction of the device.
3. Observations on the operation of the aspiration device after the first iteration.

After those objectives were carried out the following conclusions arise, regarding the room for improvements for a second iteration.

1. The selection of a back-curved centrifugal blower with design parameters that emerged from the theoretical air-speed triangles proved to be successful, as this approach provided an initial design iteration capable of achieving the transportation of solid particles. However, further

improvement involves conducting measurements of the impeller's Head under a set of flow rates to extract the real characteristic curve of the impeller, along with the efficiency of the impeller.

Furthermore, the optimization process should include a more thorough study of the effects of volute design parameters, such as the width and exit cross-section, which were excluded from the theoretical analysis. These parameters were instead chosen based on mere observation to match the dimension of casings that hold relatively similar in size impellers. The only parameter design that was involved in the theoretical analysis was the logarithmic spiral of the casing. However, the parameters for design of the spiral involve the values of the air-speed triangles. In the analysis, the theoretical air-speed triangle values were used for the first iteration, leaving room for improvement by incorporating actual values obtained after the initial iteration.

2. The mechanical components' formation that was described in the manufacturing process chapters had as primary criteria the optimization of the flow. In particular the formation of the hose diffuser with the elliptical-end shape and 45^0 bend, as well as the impeller's shroud formation along with the inlet diffuser guiding smoothly the 90^0 turn of the airstream (as seen on the following figure) are critical in the mitigation of pressure losses and sustaining a uniform flow profile. In practice, these components did not achieve the desired formation due to challenges in the manufacturing process arising from the lack of specialized tools required to implement the theoretical designs. Consequently, there is significant room for improvement in the construction of these components to better align with the documented geometry.

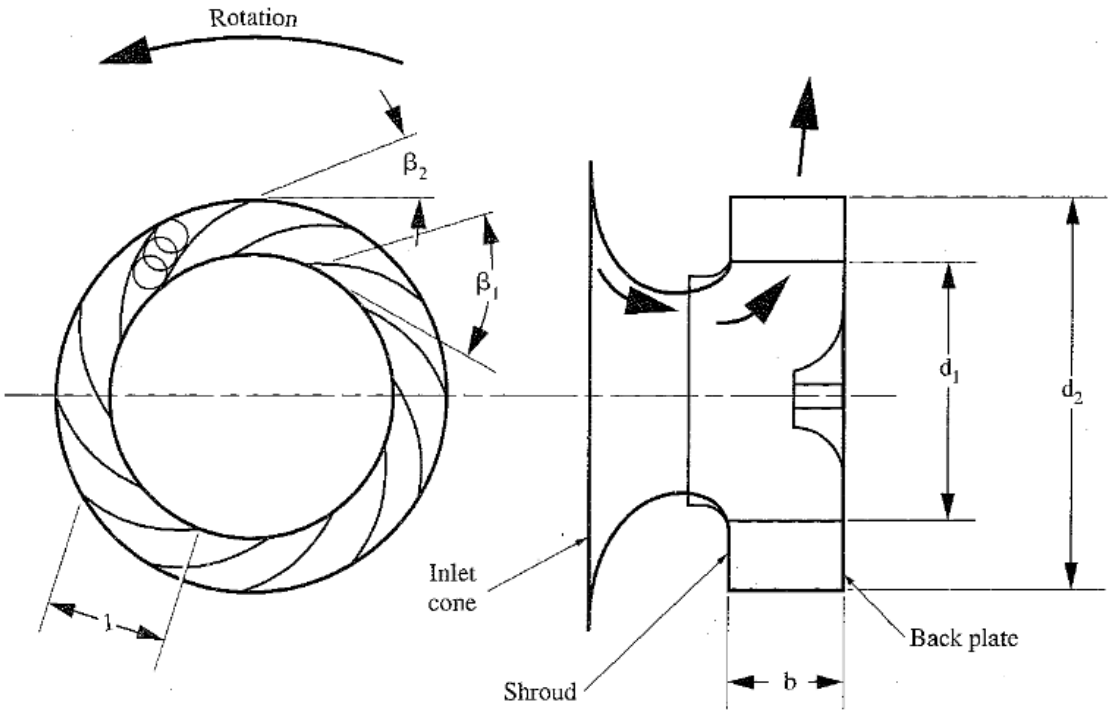

Figure 63: The importance of the curvature at the inlet cone is highlighted at the right sketch, as it provides guidance to the air flow for a smooth and efficient transition.

Lastly, the fact that all the components are modelled and assembled in CAD software facilitates the first step for an air flow simulation that may provide further insights into regions of the air channels that might require further improvement.

3. Although some useful parameters were collected after the operation of the actual device, like the solid mass flow and the air speed at the hose end when no solid particles pass through, they do not yet complete the puzzle. The key parameter is the solid particles velocity c, which will enable the calculation of the voidage ε. This, in turn, will allow for the determination of the actual air velocity and the crucial friction and impact factor λ_Z^*. Once these parameters are obtained, the system's pressure loss can be accurately modelled by combining the parameters currently available from operation.

The three points outlined above provide clear pathways for optimizing the aspiration device. Some of these points have straightforward solutions, such as integrating specialized tooling for more precise manufacturing, while others require the development of appropriate and feasible experimental methods for calculating the desired quantities.

The comparison between the aspirator device with a cyclone and with a rectangular box respectively, in regards of performance, the designing and manufacturing process, showed that the rectangular box aspirator device is a better solution. It has better performance, as it achieves higher solid mass flow rate, therefore greater productivity with relatively same free air velocity. In addition, it has less demanding process of designing parameter selection and less complexity in the manufacture process, as the geometry is simpler. Also, it has a less demanding modelling process. Therefore, this setup will go to the next design iteration process.

Finally, in the conclusions of this project are also incorporated the designing parameters of the impeller of the aspirator device with a rectangular box found in *Table 9*, as well as the operational data from this aspirator device, which can be found in *Table 10*.

Bibliography

1. D. Yang, G. Li, Y. Wang, Q. Wang, J. Li, “Prediction of Horizontal Pneumatic Conveying of Large Coal”, *Powder Technology*, 343, pp. 599-606, 2019.

2. L. M. Gomes, A. L. Amarante Mesquita, “On the prediction of pickup and saltation velocities in pneumatic conveying”, Brazilian Journal of Chemical Engineering, 31(1), pp. 35–46, 2014

3. D.M. Cook, D. Hastie, T. Hicks, P. Wypych, “A Novel Approach to Rotary Valve Venting”, University of Wollongong, Conference contribution, 2004. https://hdl.handle.net/10779/uow.27693747.v1

4. A. Gjeta, “Effect of clearance gap in spiral casing design of a centrifugal fan with optimized impeller” *European Journal of Engineering and Technology Research*, 4(9), pp. 181–185, 2019.

5. L.M. Gomes, A.L. Amarante Mesquita, “On the prediction of pickup and saltation velocities in pneumatic conveying”, *Brazilian Journal of Chemical Engineering*, 31(1), pp. 35–46., 2014.

6. G.E. Klinzing, F. Rizk, R. Marcus, L.S. Leung, *Pneumatic Conveying of Solids*, Springer, 2010.

7. H. Konno, S. Saito, “Pneumatic conveying of solids through straight pipes”, *Journal of Chemical Engineering of Japan*, 2(2), pp. 211–217, 1969.

8. S.D. Kyparissis, E. Douvi, E. Panagiotopoulos, D.P. Margaris, A. Filios, “Parametric study performance of a centrifugal pump based on simple and double arc design methods”, 3rd International Conference on Experiments/Process/System Modeling/Simulation & Optimization (IC-EpsMsO), 2009.

9. D. Misiulia, G. Lidén, S. Antonyuk, “Secondary Lip Flow in a Cyclone Separator*”, Flow, Turbulence and Combustion*, 110(3), pp. 581–600, 2023.

10. F.P. Bleier, *Fan Handbook: Selection, Application, and Design*, McGraw-Hill, 1997.

11. A. Khadivi, et al., “Identification of the promising olive (Olea europaea L.) cultivars”, *Food Science & Nutrition*, 10(4), pp. 1299–1311, 2022.

12. A. Joseph, P.A. Raj, S. Harinarayanan, T. Thomas, “Design of Pneumatic Conveying System”, *International Journal for Innovative Research in Science & Technology*, 3(11), pp. 246–251, 2017.